Crossing hydrological and geochemical modeling to understand the spatiotemporal variability of water chemistry in a headwater catchment (Strengbach, France)

Julien Ackerer, Benjamin Jeannot, Frederick Delay, Sylvain Weill, Yann Lucas, Bertrand Fritz, Daniel Viville, François Chabaux

Laboratoire d'Hydrologie et de Géochimie de Strasbourg, Université de Strasbourg, CNRS, ENGEES, 1 rue Blessig, 67084 Strasbourg Cedex, France

*Corresponding authors:

Julien Ackerer (julien.ackerer@orange.fr), Benjamin Jeannot (bjeannot.pro@gmail.com), Frederick Delay (fdelay@unistra.fr), François Chabaux (fchabaux@unistra.fr)

Abstract

Understanding the variability of the chemical composition of surface waters is a major issue for the scientific community. To date, the study of concentration-discharge relations has been intensively used to assess the spatiotemporal variability of the water chemistry at watershed scales. However, the lack of independent estimations of the water transit times within catchments limits the ability to model and predict the water chemistry with only geochemical approaches. In this study, a dimensionally reduced hydrological model coupling surface flow with subsurface flow (i.e., the Normally Integrated Hydrological Model, NIHM) has been used to constrain the distribution of the flow lines in a headwater catchment (Strengbach watershed, France). Then, hydrogeochemical simulations with the code KIRMAT (i.e., KInectic Reaction and MAss Transport) are performed to calculate the evolution of the water chemistry along the flow lines. Concentrations of dissolved silica (H_4SiO_4) and in basic cations (Na^+, K^+, Mg^{2+}, and Ca^{2+}) in the spring and piezometer waters are correctly reproduced with a simple integration along the flow lines. The seasonal variability of hydraulic conductivities along the slopes is a key process to understand the dynamic of flow lines and the changes of water transit times in the watershed. The covariation between flow velocities and active lengths of flow lines over changing hydrological conditions reduces the variability of water transit times and explains why transit times span much narrower variation ranges than the water discharges in the Strengbach catchment. These findings demonstrate that the general chemostatic behavior of the water chemistry is a direct consequence of the strong hydrological control of the water transit times within the catchment. Our results also show that a better knowledge of the concentration-mean transit time relations (C-MTT relations) is an interesting new step to understand the diversity of C-Q shapes for chemical elements. The good matching between the measured and modeled concentrations while respecting the

water-rock interaction times provided by the hydrological simulations also shows that it is possible to capture the chemical composition of waters using simply determined reactive surfaces and experimental kinetic constants. The results of our simulations also strengthen the idea that the low surfaces calculated from the geometrical shapes of primary minerals are a good estimate of the reactive surfaces within the environment.

1- Introduction

Understanding the effects of ongoing climatic changes on the environment is a major issue for the coming years. The global increase of temperature is expected to affect the hydrological cycle at a large scale, and providing a precise estimation of its repercussion on the evolution of soils and on the chemistry of waters remains difficult. This challenge results from the wide diversity of hydrological, geochemical, and biological processes, and of their coupling, that operate at the Earth's surface (e.g., Gislason et al., 2009; Goddéris et al., 2013; Beaulieu et al., 2012; 2016). Up today, the study of concentration-discharge relations (C-Q relations) has been intensively used to assess the coupling between hydrological and geochemical processes at the hillslope or watershed scales (Godsey et al., 2009; Kim et al., 2017; Ameli et al., 2017; Diamond and Cohen, 2018).

C-Q relations are acknowledged to integrate critical zone structure, the hydrological dynamics and the geochemical processes of watersheds (Chorover et al., 2017). Recent studies debated to which extend the chemical variability of waters is explained by a mixing of different water sources (Zhi et al., 2019), the chemical contrasts between deep and shallow waters (Kim et al., 2017), the variability of transit times (Ackerer et al., 2018) and/or seasonally variable flow paths (Herndon et al., 2018). It is clear that a good knowledge of the water flow paths and of their seasonal variability is an important new step to better constrain the water transit times

within catchments, and then, to correctly understand the temporal fluctuations of the composition of waters. Modeling such variability of water flow paths and water geochemical composition would require further development of modeling approaches able to combine hydrological and geochemical processes (e.g. Steefel et al., 2005; Kirchner, 2006).

Recent efforts in hydrological modeling were conducted to develop spatially distributed approaches that better consider the interplay between surface and subsurface processes (e.g., Gunduz and Aral, 2005; Kampf and Burges, 2007; Camporese et al., 2010). Due to the complexity of flows in the hydrological processes, many modeling approaches are based on the full resolution of Richard's and Saint Venant equations to correctly describe the interactions between stream, overland and subsurface waters (Kampf and Burges, 2007). These approaches have shown their ability to capture the hydrological functioning of various watersheds, knowing that the full resolution of Richard's and Saint Venant equations requires long computational times and faces calibration and parameterization difficulties (Ebel and Loague, 2006; Mirus et al., 2011). Questions have been raised regarding the optimal complexity of the equations that are needed to correctly treat the hydrology of catchments in their surface and subsurface compartments with reasonable computation times (Gunduz and Aral, 2005).

Low-dimensional models have attracted growing interest because they represent an interesting compromise between equation complexity, computational time, and result accuracy (Pan et al., 2015; Hazenberg et al., 2016; Weill et al., 2013; 2017; Jeannot et al., 2018). The reduction of dimensionality is mainly associated with a subsurface compartment (including both the vadose and the saturated zones) modeled as a two-dimensional layer. Some low-dimensional models, as the one employed in this study, can solve subsurface flow

via an integrated Richard's equation, meaning that flow and transport processes are integrated over a vertical direction or a direction normal to bedrock, and manipulate averaged (integrated) hydrodynamic properties. This type of low-dimensional approach recently demonstrated its ability to reproduce the results from fully dimensioned approaches in small catchments while reducing computational costs (Pan et al., 2015; Jeannot et al., 2018). Nonetheless, the water transit times calculated from these depth-integrated models are rarely confronted with the water-rock interaction times inferred from hydrogeochemical modeling of water chemistry in watersheds.

For its part, the understanding of the hydrogeochemical functioning of the critical zone has been significantly advanced by the implementation of reactive-transport laws in geochemical modeling codes (Steefel et al., 2005; Lucas et al., 2010; 2017; Goddéris et al., 2013; Li et al., 2017). These developments allow for considering a variety of processes, such as flow and transport processes, ion exchanges, biogeochemical reactions, and the interplay between primary mineral dissolution and secondary mineral precipitation (Moore et al., 2012; Lebedeva and Brantley, 2013; Ackerer et al., 2018). Reactive transport models have been used to explore a wide variety of scientific issues, including the study of global atmospheric CO_2 consumption by weathering reactions (Goddéris et al., 2013; Li et al., 2014), the formation and evolution of soil and regolith profiles (Maher et al., 2009; Navarre-Sitchler et al., 2009; Lebedeva and Brantley, 2013), and the variability of water quality and chemistry in the environment (Lucas et al., 2010; 2017; Ackerer et al., 2018). However, these approaches usually rely on a simple 1D flow path through a regolith column or along a hill slope to model flow in the system (e.g. Maher, 2011; Moore et al., 2012; Lucas et al., 2017; Ackerer et al., 2018). 1D reactive-transport models are useful to discuss the key processes involved in the regolith formation and in the acquisition of the water chemical composition, but these models

cannot consider the complexity of the flow trajectories in watersheds, and hence, its effects on the water chemistry.

A new step is therefore necessary for the development of hydrogeochemical modeling approaches that are applicable at the watershed scale and are able to integrate the complexity of the water flows and the diversity of the water-rock interaction processes. Recent efforts have been undertaken in the direction of merging hydrological and geochemical codes, with for example, the parallel reactive transport code ParCrunchFlow (Beisman et al., 2015), or the coupled hydrogeochemical code RT-Flux-PIHM (Bao et al., 2017; Li et al., 2017). As an alternative to fully dimensioned codes, this work proposes an original low-dimensional approach, with relatively short computation times and applicable at the watershed scale. This study is combining for the first time in this manner the results from a hydrological low-dimensional (depth-integrated for the subsurface) but spatially distributed model (NIHM) with a reactive-transport model (KIRMAT). The combination allows for simulating over time and space the flow trajectories, the flow rates, the weathering reactions, and the evolution of the water chemistry within a headwater system, the Strengbach catchment.

This catchment is one of the reference observatories of the French critical zone network (OZCAR), where multidisciplinary studies, including hydrological, geochemical and geological investigations, have been performed since 1986 ("Observatoire Hydrogéochimique de l'Environnement", OHGE; http://ohge.unistra.fr; El Gh'Mari, 1995; Fichter et al., 1998; Viville et al., 2012; Gangloff et al., 2014; 2016; Prunier et al., 2015; Pan et al., 2015; Ackerer et al., 2016; 2018; Beaulieu et al., 2016; Chabaux et al., 2017; 2019; Schmitt et al., 2017; 2018; Daval et al., 2018; see also Pierret et al., 2018 for an updated overview of the Strengbach watershed).

2- Site presentation and data acquisition

The Strengbach catchment is a small watershed (0.8 km²) located in the Vosges Mountains of northeastern France at altitudes between 883 and 1147 m. Its hydroclimatic characteristics can be found in Viville et al. (2012) or in Pierret et al. (2018). It is marked by a mountainous oceanic climate, with an annual mean temperature of 6 °C and an annual mean rainfall of approximately 1400 mm, with 15 to 20% falling as snow during two to four months per year. The snow cover period is quite variable from year to year, and may not be continuous over the entire winter. The annual mean evapotranspiration is of approximately 600 mm, and the annual mean infiltration (no significant surface runoff observed) of approximately 800 mm (Viville et al., 2012). The watershed is currently covered by a beech and spruce forest. The bedrock is a base-poor Hercynian granite covered by a 50 to 100 cm-thick acidic and coarse-in-texture soil. The granitic bedrock was fractured and hydrothermally altered, with a stronger degree of hydrothermal overprinting in the northern than the southern part of the catchment (Fichter et al., 1998). The granite was also affected by surface weathering processes during the Quaternary (Ackerer et al., 2016). The porous and uppermost part of the granitic basement constitutes an aquifer from 2 to approximately 8 m thickness. In the Strengbach watershed, the major floods and high-flow events usually occur during snowmelt periods at the end of the winter season or in the early spring. By contrast, the low-flow periods commonly happen at the end of the summer or during the autumn. Several springs are captured for drinkable water supply directly in the subsurface by small collectors (figure 1). The watershed has been equipped with several piezometers and boreholes since 2012, those being located along the slopes on both sides of the watershed (figure 1 in Chabaux et al., 2017).

Spring waters have been regularly collected and analyzed since 2005, with monthly sampling supplemented by a few specific campaigns to cover the complete range of water discharges in the watershed. Piezometer waters have been collected only during specific sampling campaigns over the period 2012-2015, and, as for the spring waters, these sampling campaigns cover different hydrological conditions from wet to dry periods. The soil solutions were collected with a monthly frequency on the southern slope at a beech site (named HP) and to the north at a spruce site (named VP; figure 1; more details in Prunier et al., 2015). For all the collected waters, the concentrations of the major dissolved species and the pH were determined by following the analytical techniques used at LHyGeS (Strasbourg, France) and detailed in Gangloff et al. (2014) and Prunier et al. (2015). Discharges of water from the springs were measured during the sampling campaigns, as were the water levels within the piezometers.

The mineralogy and the porosity of the bedrock have been studied in detail in previous studies (El Gh'Mari, 1995; Fichter et al., 1998). On the southern part of the catchment, the weakly hydrothermally altered granite (named HPT, figure 1) is mainly composed of quartz (35%), albite (31%), K-feldspar (22%) and biotite (6%). It also contains small amounts of muscovite (3%), anorthite (2%), apatite (0.5%) and clay minerals (0.5%). On the northern part of the catchment, the lithology is more variable, with the presence of gneiss close to the crest lines and the occurrence of hydrothermally altered granite on the rest of the slopes (El Gh'Mari, 1995, figure 1).

The hydrological, geochemical and petrological data obtained from these field investigations are the basis of the modeling exercise presented in this study. More precisely, this study is based on hydrogeochemical data from 2005 to 2015 for waters from four springs of the

185 southern part (CS1, CS2, CS3 and CS4) and one spring of the northern part (RH3) of the
186 watershed (figure 1). Hydrogeochemical data obtained over the period 2012-2015 for two
187 piezometers (PZ3, PZ5) of the southern part of the watershed are also studied (figure 1). The
188 overall hydrogeochemical database is available as supplementary tables (tables EA1 to EA9).
189 The specific chemical data from spring and piezometer waters modeled in this study are
190 reported in table 1.

191 **3- Modeling methods**

192 The modeling developments presented in this study represent a new step in the efforts
193 undertaken to constrain the mechanisms controlling the geochemical composition of surface
194 waters and to understand their spatial and temporal variations at the scale of headwater
195 mountainous catchments (Schaffhauser et al., 2014; Lucas et al., 2017; Ackerer et al., 2018).
196 The main innovation of this present work is to couple a spatially distributed and low-
197 dimensional hydrological model with a reactive transport code to constrain the
198 spatiotemporal variability of chemical composition of waters. To the best of our knowledge,
199 this is the first time that such a coupling between low-dimensional hydrological and
200 hydrogeochemical modeling approaches has been attempted in this way at the watershed
201 scale.

202 **3-1 Hydrological modeling**

203 To assess the water flows in the watershed, several simulations were performed with the
204 hydrological code NIHM (Normally Integrated Hydrological Model; Pan et al., 2015; Weill et
205 al., 2017; Jeannot et al., 2018). This code is a coupled stream, overland, and low-dimensional
206 (depth-integrated) subsurface flow model developed at LHyGeS and already tested in the
207 Strengbach watershed (Pan et al., 2015). The stream and overland flows are described by a

208 diffusive-wave equation, and the subsurface flow is handled through an integration (in a
209 direction normal to bedrock) of the unsaturated-saturated flow equation from the bedrock to
210 the soil surface (Weill et al., 2017). The exchanges of water between the surface and
211 subsurface flows are addressed via a first-order exchange coefficient involving the thickness
212 and the hydraulic conductivity of an interface layer (e.g., the riverbed, for interactions
213 between surface routing and subsurface compartments), and the hydraulic head differences
214 between the compartments (Jeannot et al., 2018).

215 Regarding the hydrological simulations, NIHM was used with only its stream flow and
216 subsurface flow compartments activated, the Strengbach catchment having never evidenced
217 diffuse two-dimensional surface runoff or subsurface exfiltration over large areas. In addition,
218 and because of the steep slopes, the stream flow process revealed almost insensitive to the
219 roughness and Manning's parameters of the riverbed, which were set to usual values for very
220 small streams of mountainous landscapes. By contrast, the parameters of the subsurface were
221 adjusted in NIHM through a calibration-validation process. Several zones of heterogeneity
222 (figure 2) were defined based on field observations (Ackerer et al., 2016; Chabaux et al., 2017).
223 In each of these zones, the saturated hydraulic conductivity, the depth of substratum, and the
224 porosity, were set to uniform values. Other parameters (the residual water content, the
225 specific storage, the Van Genuchten coefficients n and α, and the saturated hydraulic
226 conductivity of the interface layer between the groundwater compartment and the surface
227 compartment) were set to uniform values over the whole catchment (table 2). The thickness
228 of the aquifer that was used for the simulations varied from 2 m near the main crests to up to
229 8 m in the middle of the watershed (figure 2), in agreement with the data obtained during the
230 recent geological investigations and drilling campaigns undertaken at the catchment (Ackerer
231 et al., 2016; Chabaux et al., 2017). The uniform precipitations over space applied at the surface

of the catchment are drawn from data of the pluviometric station located at the highest elevation of the watershed (site PA, figure 1). The hydrological model NIHM was then run over a first time period (years 1996-1997). By a Monte-Carlo approach, the parameters were "randomly" sought to improve the fitting between the observed and simulated flow rates at the outlet of the catchment (table 2). The fit was quantified by the root mean square error (RMSE) and the Kling-Gupta efficiency coefficient (KGE; Gupta et al., 2009), applied to the outlet flow rate of the stream, which is the only reliable and always available hydrological variable monitored in the system.

Once the best fit was obtained, the model was then run over another time period (2010-2015), but without changing the parameters anymore, and the quality of the fit was re-assessed for this new time-period with the KGE and RMSE. Figure 2 shows the result for the 2010-2015 time period. After the water discharges were correctly reproduced at the outlet, a backtracking approach was used to identify which subsurface flow lines reach the sampled sites. To back track the water particles, the velocity fields calculated by the NIHM model were inverted in their direction, and the locations of the backtracked particles were saved at each time-step. A daily time-step was used for the backtracking, as a compromise between computational efforts and a refined description of the transient velocity fields. A schematic representation of the backtracking approach is given in figure 3. This methodology allows for constraining the flow lines that bring waters for a given time and at a given position on the catchment. This information is of major interest to determine the origin of the spring and piezometer waters. It is shown at the catchment scale, that flows are mainly driven by gravity in association with the steep slopes of the watershed, the latter being almost evenly drained over its whole surface area (figure 4). For each water sampling area, ten flow lines that bring water to the

location of interest were determined (figure 4), together with a few features of the flow lines, including: local velocities, mean velocities, and length of the flow paths.

It is worth noting that NIHM is a depth-integrated model for its subsurface compartment where flow is simulated over a 2D-mesh and under the assumption of an instantaneous hydrostatic equilibrium in the direction perpendicular to the substratum. Therefore, times calculated along the backtracked streamlines correspond to a date, x days before arrival, at which a water particle entered the subsurface or passed at a given location along the streamline. Streamlines calculated via backtracking and reaching sampling sites only consider flow in the subsurface compartment and are conditional to an arrival date at a prescribed location. As backtracked streamlines are not associated with mean water flux values, the transit time distributions drawn from streamline calculations are only an approximation of the actual transit time distributions.

It should also be noted that, knowing the water head at a given location, the assumption of an instantaneous hydrostatic equilibrium over the direction perpendicular to the substratum directly renders the associated water pressure over the whole aquifer along that direction. Then, since the water pressure, saturated hydraulic conductivity, porosity, residual water content, and Van Genuchten coefficients are known, the Van Genuchten equation can be integrated numerically, which gives to NIHM the possibility to calculate local depth-integrated hydraulic conductivities over the direction perpendicular to the substratum.

With a conditioning of NIHM limited to the reproduction of the stream flow rates at its outlet, it can be questioned on the reliability of the solution, equifinalities in model outputs being usually all the more present that few data are available to condition the model. The point is that there is no other reliable information on flow patterns, and for example, the few

boreholes available (mainly drilled for rock core sampling) are deep enough to intercept a few fractures in the bedrock (under the bottom of the aquifer simulated by NIHM). This renders the water levels monitored in these open boreholes unable to reflect hydraulic pressure heads in the active shallow porous aquifer of the catchment. Nevertheless, the steep slopes of the catchment are the main feature conditioning water velocities, thus rendering transit times (the variable of interest for a geochemical study) very stable over time, irrespective of hydro-meteorological conditions and current head pressure in the system. After the present study was completed, NIHM was employed at the Strengbach to simulate water content distributions with the aim to mimic data from magnetic resonance sounding (Weill et al., 2019). The model was slightly improved in terms of storage and its variability over space, but the modeled distribution of flow paths, their variability, and the associated transit time distributions remained unchanged.

3-2 Hydrogeochemical modeling

The simulations of the water chemical composition along the flow lines were performed with the hydrogeochemical KIRMAT code (KInectic of Reaction and MAss Transport; Gérard et al., 1998; Lucas et al., 2010; Ngo et al., 2014; Lucas et al., 2017). KIRMAT is a thermokinetic model derived from the Transition State Theory (TST, Eyring, 1935; Murphy and Helgeson, 1987) that simultaneously solves the equations describing geochemical reactions and transport mass balance in a 1D-porous medium. The mass transport includes the effects of one-dimensional convection, diffusion and kinematic dispersion. Chemical reactions account for the dissolution of primary minerals and oxido-reduction reactions, in addition to the formation of secondary minerals and clay minerals. KIRMAT includes the oxido-reduction processes of iron (Fe), sulfur (S) and other important species for the corrosion of iron (Ngo et al., 2014). Oxido-reduction reactions are

handled through Nerst equations (Gerard et al., 1998; Ngo et al., 2014). The calculation of the dissolution rates of primary minerals is based on the TST and on a kinetic law (equation 1 in Ackerer et al., 2018, equation 1 in Ngo et al.,2014). Thermodynamic and kinetic data for the primary minerals are available in supplementary materials (supplementary tables EA10, EA11 and EA12).

The clay fraction is defined as a solid solution made up of a combination of pure clay end-members. The clay end-members are defined on the basis of X-ray diffraction analyses of clay minerals present in bedrock samples collected in the field (Fichter et al., 1998; Ackerer et al., 2016; 2018). They consist of K-Illites, Mg-Illites, Ca-Illites, Montmorillonites, Na-Montmorillonites, K-Montmorillonites, Ca-Montmorillonites and Mg-Montmorillonites (supplementary material table EA13). During the hydrogeochemical simulations, the clay solid solution is precipitated at thermodynamic equilibrium and precipitation is not described by a kinetic law. The amount of a given clay mineral precipitated at any step of the simulated reaction is calculated to maintain the chemical equilibrium from the moment it is reached in the geochemical reaction. The amount of clay precipitated depends on the solubility product (K) of the clay end members (Tardy and Fritz, 1981). This multicomponent solid solution reproduces the impurity of the clay minerals formed during low-temperature water-rock interactions (Tardy and Fritz, 1981), and its composition varies over time, depending on the evolution of the water chemistry and the bedrock mineralogy (Ackerer et al., 2018). For the secondary minerals other than clay minerals, the precipitation rates are derived from TST and described by a kinetic law (equation 2 in Ngo et al., 2014). Precipitation of typical secondary minerals such as carbonates, hematite or amorphous silica was tested, but these minerals were not formed given the saturation states calculated in the geochemical modeling (supplementary table EA14). Secondary mineral precipitation is therefore controlled by clay mineral formation.

The KIRMAT code also includes feedback effects between mineral mass budgets, reactive surfaces, and the evolution of bedrock porosity (Ngo et al., 2014). The reactive surfaces of the primary minerals were calculated by assuming a simple spherical geometry for all the minerals, and the mean size of the minerals was estimated from the observation of thin sections from bedrock samples. During simulations, clay mineral precipitation and the evolution of the reactive surfaces of primary minerals are tracked together with chemical processes and water chemical composition. Given the short time scales reported by the hydrological simulations (monthly timescale), changes in the reactive surfaces of primary minerals over the simulation time were negligible. The KIRMAT code has already been applied in geochemical modeling of alluvial subsurface waters (Lucas et al., 2010) and surface waters (Lucas et al., 2017; Ackerer et al., 2018).

For this study, the modeling strategy is adapted from Ackerer et al. (2018) to consider the new transit time constrains provided by the hydrological code NIHM. To capture the chemical composition of the spring and the piezometer waters, numerical simulations were performed along the subsurface streamlines that were determined through the backtracking approach. A sketch of the hydrogeochemical modeling strategy is provided in figure 5. For each streamline, several KIRMAT simulations were performed with different starting positions along the active part of the line. The starting positions represent the locations at which the soil solutions percolate through the subsurface shallow aquifer. These starting positions are spaced with a constant lag distance of 1 m along the subsurface streamlines, which results in a sub-continuous percolation of solutions along the whole length of the lines. The deepest soil solutions collected to the south at the beech site (HP) and to the north at the spruce site (VP) were considered representative of the soil solutions for the southern and northern slopes of the catchment, respectively. The data of soil solution chemistry used in this study are available

348 in Prunier et al. (2015) and in supplementary tables (tables EA6 and EA7). These soil solutions
349 integrate the surface processes occurring before water percolation into the weathered
350 bedrock (regolith). Because the soil solutions can be injected into the aquifer at various times,
351 the temporal variability of the soil solution chemistry and its impact on the water-rock
352 interactions along the flow paths are accounted for in the modeling approach.

353 Data related to the regolith properties, such as the mineralogical compositions, the mineral
354 reactive surfaces and the thermodynamic and kinetic constants are given in Ackerer et al.
355 (2018) and in supplementary tables (tables EA10 to EA14). Mineral phases are assumed
356 homogeneously distributed over the regolith layer. By following this strategy, the simulations
357 that consider soil solutions percolating at the upper part of the catchment reflect the chemical
358 evolution of waters with long path lengths and long transit times within the aquifer. By
359 contrast, shorter path lengths and shorter transit times are associated with the percolation of
360 soil solutions that occurs in the vicinity of the sampling locations (figure 5). Because the springs
361 or the piezometers collect waters from different origins and with various transit times,
362 integration along each water flow line was performed. The aim of the integration is to
363 determine the mean chemical composition resulting from the mixing of the waters
364 characterized by variable transit times (figure 5). The integrated chemical composition of the
365 waters provided by a given flow line is calculated by taking the arithmetic mean of the solute
366 concentrations calculated by the succession of the KIRMAT simulations along the flow line
367 (figure 5). This arithmetic mean reflects a simple full mixing of uniform water fluxes along a
368 stream line irrespective of the short or long transit times. In other words, the geochemical
369 simulations are based on the hypothesis of spatially homogenous water-rock interactions
370 along the flow lines. The soil solutions are assumed to percolate uniformly within the aquifer
371 and are then conveyed along the slopes by uniformly distributed masses of water until

372 reaching the sampling locations. When needed, the eventual calculation of water chemistry
373 exiting several stream lines reaching a sampling location accounts for the spreading associated
374 with various flow paths, spatial variability of water velocities and related travel times.

375 **4- Hydrological modeling results**

376 **4-1 Spatial variability of the flow lines**

377 The results provided by the hydrological code NIHM show that to the first order, the
378 Strengbach catchment is well drained and that the topography exerts an important control on
379 the flow line distribution (figure 4). Along the hillsides presenting linear or slightly convex
380 slopes, the water flow lines show simple characteristics. The flow paths are nearly parallel,
381 and the water velocities are similar along the different flow lines on this type of hillside. The
382 water velocities tend to increase when moving downstream, with slower velocities near the
383 main crests and higher velocities on the steepest parts of the hillsides. The waters collected
384 along this type of hillside are therefore characterized by small variability of transit times. This
385 is the case for the CS1, CS3 and RH3 spring waters located on the southern and northern parts
386 of the catchment (figure 4). This is also the case for the piezometers PZ3 and PZ5 in the
387 southern part of the watershed (figure 4). For the sites located on linear or slightly convex
388 slopes (CS1, CS3, RH3, PZ3 and PZ5), all the characteristics of the different flow lines that feed
389 each site are therefore comparable for a given site and for a given date.

390 By contrast, in the vicinity of the valley and in the topographic depressions, the hydrological
391 modeling indicates that the flow line characteristics are more variable. Because flow lines
392 coming from different hill-sides can feed a topographic depression, mixing of different flow
393 lines with variable flow paths and contrasted water velocities can occur at these locations.
394 The waters collected in valleys or in topographic depressions are therefore characterized by a

higher variability of transit times. This is the case for the CS2 and CS4 springs, which are located in a depression, in the axe of the small valley, and surrounded by slopes with various orientations, and a complex flow line distribution (figure 4). For these two springs, the characteristics of the different flow lines can be different for a given date.

4-2 Temporal variability of the flow lines

Hydrological modeling under general transient conditions can render the evolution over time of water flows in the watershed but also of other hydraulic variables. As an example, after an important rainfall event (30/03/2010 in figure 6), snapshots of the integrated hydraulic conductivity (modeled via the Van Genuchten formulation) in the subsurface and simulated by NIHM at the scale of the mesh size show increasing values with decreasing elevation in the watershed. The same observation holds for conductivities during drought periods (see 29/11/2011, in figure 6). Provided that the hydraulic head gradient is largely dominated by the topography and therefore almost constant over time (figure 6), the water velocities are increasing along the flow lines from crests to valleys, irrespective of the wet versus dry hydrological periods. However, it is noticeable that wet periods are favorable to a large extension in the valleys of high values of depth averaged hydraulic conductivity indicating that the aquifer is locally almost completely saturated from bottom to top (e.g., values of 6.5×10^{-5} ms^{-1} in figure 6 for a saturated bound at $8\ 10^{-5}$ ms^{-1}).

For the CS1 spring, the mean flow velocities along the flow lines vary from approximately 1 m/day to 7 m/day between the severe drought of 29/11/2011 and the strong flood of 30/03/2010 (figures 7A and 7B). These events correspond to the annual minimum and maximum flow rates at the outlet of the Strengbach watershed. For the same dates, the mean velocities vary from 2 – 12 m/day, 1 – 4 m/day and 1 – 9 m/day for the springs CS2, CS3 and

418 CS4, respectively. The variations from drought to flood are very similar for the piezometer
419 waters, with velocities in the ranges 2 – 10 m/day and 2 – 12 m/day for the PZ3 and PZ5
420 piezometers, respectively. The RH3 spring located on a steeper part of the northern slopes
421 exhibits flow velocity variations from 5 to 20 m/day from dry to flood conditions.

422 In addition to the flow velocity variations, the hydrological simulations also reveal variability
423 in the lengths of the active parts of the flow lines. For illustration, the active parts of the flow
424 lines are reduced from 160 m to 110 m from the flood to the drought events for the CS1 spring
425 (figures 7A and 7B). Such variability is triggered by the particular seasonal variations of the
426 hydraulic conductivities within the catchment. After important precipitations, high water
427 content and large integrated hydraulic conductivities (sometimes up to the saturated bound)
428 are simulated in the vicinity of the crests and all along the small valley of the catchment (figure
429 6). During periods of drought, the simulations indicate a strong decrease of hydraulic
430 conductivities close to the main crests and much smaller variations at mid-slopes (figure 6).
431 The crests rapidly dry out, whereas the areas at mid-slopes still supply some water to the
432 stream network. These contrasting hydrological behaviors result from the differences in
433 aquifer thickness and water storage between the crests and the other parts of the catchment
434 (figure 2). Thin aquifer, flow divergence and absence of feeding areas prevent large water
435 storage on the crests, in opposition to mid-slope parts with much thicker aquifers and the
436 presence of feeding areas upstream. This particular pattern simulated for the hydraulic
437 conductivities implies that the active parts of the flow lines extend up the main crests during
438 important floods, whereas they are limited to mid-slopes after a long dry period.

439 The consequence of this hydrological functioning is to moderate the seasonal variations of the
440 transit times of waters, as the active lengths of flow lines vary simultaneously with water flow

441 rates. Calculations indicate that for the spring and piezometer waters collected in this study,
442 the mean transit times of waters only vary from approximately 1.75 to 4 months between the
443 strongest flood and the driest conditions. Notably, these short subsurface water transit times
444 are explained by the small size of the catchment and the steep slopes.

445 **5- Hydrogeochemical modeling results**

446 **5-1 CS1 and CS3 springs (southern slope)**

447 The CS1 and CS3 springs emerge on the same slope and drain the same rocks. Their
448 hydrological behavior is also very similar in terms of flow lines and water transit times. The
449 interesting consequence of the simple flow line distribution for these springs is that a single
450 flow line can be considered as representative of all the flow lines that are feeding the spring,
451 irrespective of the hydrological conditions. Hydrogeochemical simulations were performed
452 along a single flow line for different hydrological periods using the methodology illustrated in
453 figure 5. The case of CS1 spring is used below to highlight the main results obtained from this
454 approach. For the strong flood of 30/03/2010, the KIRMAT simulations modeling the waters
455 coming from the vicinity of the spring and characterized by short transit times produced too
456 much diluted solutions, whereas the waters coming from the main crests were too much
457 concentrated to reproduce the spring water chemical composition. However, after an
458 integration of all the waters arriving at CS1 with the different transit times employed for the
459 simulation, the resulting geochemical composition correctly reproduces the chemical
460 composition of CS1 spring water at this date (H_4SiO_4, Na^+, K^+, Mg^{2+}, and Ca^{2+} concentrations,
461 figure 7D). A similar conclusion is obtained for the important drought of 29/11/2011. Again,
462 geochemical integration of all the waters arriving at CS1 along a water line but with different

463 transit times correctly reproduces the chemical composition of the CS1 spring waters collected
464 on this date (figure 7C). This comment applies regardless of the time period considered.

465 The coupled hydrological and hydrogeochemical approach has been applied for the CS1 spring
466 for 6 dates covering the whole range of the water discharges of the spring (table 1). The
467 modeling results capture the seasonal variations of the water chemical composition of the CS1
468 spring over the whole range of observed flow rates at CS1 (figure 8). Simulations especially
469 reproduce the 20-30% variation in H_4SiO_4 concentrations (figure 8A), the 10-20% variation in
470 Na^+ concentrations (figure 8C), and the relatively stability of the K^+, Mg^{2+} and pH of the CS1
471 waters (figure 8E, 8F and 8D). The response of each chemical element to a change in water
472 discharge is related to the initial soil solution concentration, the nature of primary minerals
473 controlling its budget and the degree of its incorporation into clay minerals. Specific
474 concentration-mean transit time relations (C-MTT relations) explain why the response of
475 solute concentrations to hydrological changes (C-Q relations) is different for each element
476 (figure 9). Similar results are obtained for the CS3 spring (figure EA1), showing, as for the CS1
477 spring, that the model correctly simulates the water chemical composition of the CS3 spring.

478 Because the lengths of the flow lines vary over time, the patterns of dissolution rates for
479 primary minerals and precipitated amount of clay minerals are mainly controlled by the spatial
480 and temporal variability of the flow lines. During wet conditions, the upper parts of the
481 catchment are the areas of maximal dissolution rates of primary minerals and of maximal
482 formation of clay minerals in the regolith. During dry conditions, the dissolution and
483 precipitation are maximal at mid-slopes, as the upper parts of the catchment are simply dry.

484 **5-2 PZ3 and PZ5 piezometers (southern slope)**

485 The two piezometers PZ3 and PZ5 are located on the southern part of the catchment, and
486 their waters drain a granitic bedrock similar to that drained by the CS sources. As for the CS1
487 and CS3 springs, the NIHM modeling results show that the flow lines arriving at the PZ3
488 piezometer are characterized by a relatively simple distribution (figure 4). For the PZ5
489 piezometer located downstream, the flow lines cover a larger area on the slope, especially
490 during droughts (figure 4). However, for a given date, all the flow lines show similar velocities,
491 with particularly fast flow in the lower portion of the hillslope. These results imply that, as for
492 the CS1 and CS3 springs, the hydrogeochemical simulations of PZ3 and PZ5 piezometer waters
493 can be performed by relying upon a single flow line representative of all the waters collected
494 by the piezometers on a given date. The geochemical integration is able to reproduce the
495 chemical composition of the waters of the two piezometers, as illustrated in figure 10 for the
496 flood of the 05/05/2015 and in figure EA2 for the dry conditions of 10/11/2015. Together,
497 these modeling results show that the flow along linear or slightly convex slopes on the
498 southern part of the catchment allows to correctly capture the water chemistry of each
499 sampling site with a straightforward integration along a single and representative flow line.

500 **5-3 The CS2 and CS4 springs (in the valley axe)**

501 CS2 and CS4 spring waters drain the same granitic bedrock as the CS1 and CS3 waters, but are
502 located in the direction of the small valley of the Strengbach stream and surrounded by slopes
503 of various orientations and inclinations (figure 4). Consequently, the distribution of the flow
504 lines is much more scattered than for the CS1 and CS3 springs. For the CS2 spring, and for all
505 the hydrological conditions, two different groups of flow lines have been determined by the
506 backtracking approach: a northern group characterized by relatively slow velocities and a
507 southern group with higher velocities (figure 4 and figures 11A, 11B). This scattered

distribution of the flow lines implies that a single specific flow line cannot be representative of all the waters collected by the spring. The flow lines calculated using the NIHM model allow for constraining the trajectories of the waters within the watershed; however, the simulations performed in this study cannot provide the mass fluxes of water carried by each flow line. Consequently, a straightforward calculation of the chemistry of the CS2 spring, such as depicted above for CS1, is not applicable because the mixing proportions between the different flow lines are unknown.

Alternatively, it is possible to determine the concentrations in the waters carried by the slowest and the fastest flow lines that are feeding the spring and to compare the results with the observed chemistry of the spring water. The results indicate that for all the hydrological conditions, the concentrations calculated from the geochemical integration along the slowest and the fastest flow lines are able to correctly frame the chemical composition in terms of H_4SiO_4, Na^+, K^+, Mg^{2+}, and Ca^{2+} of the CS2 spring waters (results are reported for H_4SiO_4 and Na^+ in figures 11C and 11D). The modeling results for CS2 also suggest that the contributions of the slow and fast flow lines are comparable over most of the hydrological conditions, as the observed concentrations are in general at the midpoint between the min (i.e., fast) and max (i.e., slow) boundaries (figures 11C and 11D). It is only for the important droughts that the spring chemistry seems to be mainly controlled by the southern and faster group of flow lines. Further works to precisely estimate the mass fluxes of water carried by each flow line are necessary to model the chemistry of the CS2 spring water with a weighted mixing calculation. The same conclusions apply to the CS4 spring located close to CS2.

5-4 The RH3 spring (northern slope)

530 The RH3 spring is located on the northern part of the catchment (figure 4), where steep slopes
531 imply fast water velocities and subparallel flow lines. However, if the distribution of the flow
532 lines on the RH3 hillside is simple (as for the CS1 and CS3 springs) the precise lithological
533 nature of the bedrock drained by the RH3 waters is more difficult to constrain (Ackerer et al.,
534 2018). Unlike the southern slope, the bedrock of the northern part of the catchment reveals
535 a complex lithology, with gneiss outcropping in the upper part of the slope and granite of
536 variable degree of hydrothermal overprinting in the intermediate and lower parts. These
537 lithological variations can explain the differences in chemical composition between the RH3
538 spring waters and the waters of the southern part of the catchment: the RH3 spring waters
539 are characterized by systematically higher concentrations of K^+ and Mg^{2+} cations but show
540 similar concentrations for the other major elements (Ackerer et al., 2018; Pierret et al., 2018).
541 The vertical extension of the gneiss and the spatial variability of the hydrothermal overprinting
542 along the northern slopes are not well known, with the consequence that a straightforward
543 modeling of water chemistry as done for CS1 is not possible for RH3.

544 Alternatively, simulations of two extreme cases can be performed by assuming that the flow
545 lines only run, either on gneiss or on hydrothermally altered granite. When only considering
546 the hydrothermally altered granite (VS facies), the simulated concentrations of H_4SiO_4 and Na^+
547 are close to the measured ones. Nevertheless, the concentrations of K^+ and especially Mg^{2+}
548 are clearly underestimated (figure 12B). In the case of the flow lines only running on gneiss
549 (GN facies), the simulated concentrations of H_4SiO_4 and Na^+ also match the data. However,
550 due to the higher abundance of biotite in the gneiss, the simulated concentrations of K^+ and
551 Mg^{2+} are higher than the measured ones (figure 12A). At this stage, it is therefore reasonable
552 to propose that the chemical composition of the RH3 spring waters reflects mixing of the two
553 lithological influences. By assuming a geochemical conservative mixing, which is likely a too

554 simplistic scenario, the results would indicate that the flow lines portions running on gneiss
555 and on hydrothermally altered granite count for approximately 40-50% and 50-60% of the
556 total water path length, respectively.

557 Further works to estimate the location of the contact between gneiss and granite are required
558 for more realistic modeling and hence a deeper interpretation of the chemical composition of
559 the RH3 spring waters. In any case, the important point to stress here based on the above
560 simulations is that the complex lithology and bedrock heterogeneity mainly impact the K^+ and
561 the Mg^{2+} budget of the RH3 waters, but not or only slightly the H_4SiO_4 and Na^+ concentrations,
562 which control the main part of global weathering fluxes carried by the Strengbach spring
563 waters. These results readily explain why although the RH3 spring waters exhibits higher Mg^{2+}
564 and K^+ concentrations than the other CS springs, they carry relatively similar global weathering
565 fluxes (Viville et al., 2012; Ackerer et al., 2018).

566 **6- Discussion**

567 The coupling of the NIHM and KIRMAT codes allows for building a better modeling scheme to
568 those commonly used in previous studies regarding the hydrogeochemical modeling of
569 surface waters at the watershed scale. In such previous works, the geochemical simulations
570 were performed mainly along a single 1D flow line, only characterized by homogeneous mean
571 hydrological properties (Goddéris et al., 2006; Maher, 2011; Moore et al., 2012; Lucas et al.,
572 2017; Ackerer et al., 2018). In a previous study on the Strengbach watershed (Ackerer et al.,
573 2018), the soil solutions were also assumed to percolate in the bedrock only at a single starting
574 point of the flow lines. Although these previous approaches were useful for determining the
575 long-term evolution of regolith profiles and/or the mean chemistry of waters at the pluri-
576 annual scale, they cannot be used to discuss the seasonal variations of the water chemical

577 composition. The NIHM-KIRMAT coupling approach makes this possible, as it provides the
578 spatial distribution of the flow lines at the watershed scale and their variations over time.
579 Furthermore, the proposed modeling approach also integrates a soil solution percolation
580 scheme with inlets uniformly distributed along the slope, which is more realistic than a
581 scheme assuming that each sampled site is fed by a single flow line carrying waters with a
582 unique transit time. The good agreement between modeling results and observations over a
583 large panel of hydrological conditions gives strength to the conclusions and implications that
584 can be drawn regarding the hydrogeochemical functioning of this headwater catchment.

585 **6-1 Choices of the reactive surfaces and the kinetic constants**

586 For the geochemical simulations performed in this study, the kinetic constants that were used
587 to describe the dissolution reactions of the primary minerals are standard constants
588 determined through laboratory experiments (supplementary table EA12). The reactive
589 surfaces of the primary minerals were calculated by assuming a simple spherical geometry for
590 all the minerals (supplementary table EA10). Over the last years, several studies have
591 suggested that the kinetic constants determined through laboratory experiments
592 overestimated the rates of the dissolution reactions in natural environments (White and
593 Brantley, 2003; Zhu, 2005; Moore et al., 2012; Fischer et al., 2014). The origin of this
594 laboratory-field discrepancy is still a matter of debate (Fischer et al., 2014). Different
595 processes have been proposed to explain the gap between laboratory and field estimates,
596 such as the crystallographic anisotropy (Pollet-Villard et al., 2016), progressive occlusion of
597 the primary minerals by clays (White and Brantley, 2003), or the formation of passivation
598 layers at the surfaces of the minerals (Wild et al., 2016, Daval et al., 2018). The difficulty to
599 reconcile field and laboratory estimates can also be related to the challenge of defining

relevant reactive surfaces at different space scales (Li et al., 2006; Navarre-Sitchler and Brantley, 2007).

The present modeling work regarding the Strengbach catchment shows that the chemical composition variability of the spring and piezometer waters is fully captured via geometric reactive surfaces and standard kinetic constants, while respecting the water-rock interaction times within the catchment. This result suggests that the mean rates of the weathering reactions employed in this modeling work are realistic, which in turn implies that the modeling approach developed in this study does not underline significant mismatches between field and laboratory reaction rates. The calculated rates of the dissolution reactions depend on the product between the kinetic constants of the reactions and the mineral reactive surfaces. In the experimental studies performed for determining the kinetic constants of dissolution reactions, the constants are usually determined by normalizing the experimental weathering rates with the Brunauer-Emmett-Teller surfaces determined from experiments of gas absorption (BET surfaces; Chou and Wollast, 1986; Lundstrom and Ohman, 1990; Acker and Bricker, 1992; Amrhein and Suarez, 1992; Berger et al., 1994; Guidry and Mackenzie, 2003).

In table 3, the BET surfaces are compared with the geometric surfaces of the minerals involved in the dissolution experiments, recalculated from the size ranges of the minerals. For most of the minerals (apatite, quartz, albite, K-feldspar, and anorthite), the geometric surfaces are within the same order of magnitude as the BET surfaces, even if often slightly lower (table 3). However, as the BET surfaces are determined with fairly large uncertainties, especially for low BET surfaces (up to ± 70%), and as they can be very different depending on the gas used (up to 50% of difference between N2 or Kr absorption; Brantley and Mellott, 2000), the above differences between the geometrical and the BET surfaces cannot be considered significant

for the majority of minerals used in the Strengbach simulations. A significant difference only appears for biotite, with the geometric surfaces one order of magnitude less than the BET surfaces (table 3). However, for biotite, due to its layered structure, it has been shown that approximately 80 – 90% of the surface area accessible by the gases used to estimate BET surfaces is not accessible for weathering reactions (Nagy, 1995).

The above considerations explain why for a granitic bedrock as found in the Strengbach catchment, the geometric surfaces are relevant to describe the surfaces of water-rock interactions at the space and time scales of this study. An immediate corollary is that the values of the standard kinetic constants (table EA12) are also appropriate to calculate reaction rates with mineral geometric surfaces in our modeling approach. This ability may be related to the fact that all the minerals that have been used in the dissolution experiments and in the kinetic studies were collected in the field (e.g., Acker and Bricker, 1992; Amrhein and Suarez, 1992). These minerals were likely affected by anisotropy, passivation layers, and any types of aging effects related to long-term water-rock interactions. Our results might therefore mean that the standard kinetic constants obtained in such experiments integrate the aging effects that have affected the reactivity of the primary minerals in natural environments. This would explain why it is possible to capture the full variability of the water chemistry in a headwater catchment with simple geometric reactive surfaces and standard kinetic constants.

At this stage, the results of our simulations strengthen the idea that the low surfaces calculated from the geometrical shapes of minerals provide good estimates of the reactive surfaces within this type of environment (Brantley and Mellott, 2000; Gautier et al., 2001; White and Brantley, 2003; Zhu, 2005; Li et al., 2017). They are certainly the values to be used for hydrogeochemical modeling such as that performed in this work, in addition to the use of

646 the experimental kinetic constants for mineral dissolution. These conclusions are certainly not
647 specific to the Strengbach catchment and could be applicable to many other headwater
648 granitic catchments.

649 **6-2 Implications for the acquisition of the water chemistry**

650 The results of the NIHM-KIRMAT hydrogeochemical modeling have strong implications
651 regarding the hydrogeochemical dynamic of the Strengbach watershed. This work reinforces
652 several hypotheses formulated by previous studies conducted in the Strengbach watershed
653 (Viville et al., 2012; Pierret et al., 2014; Pan et al., 2015; Chabaux et al., 2017; Weill et al., 2017;
654 Ackerer et al., 2018), but also brings new insights on the hydrogeochemical functioning of the
655 catchment. Firstly, the modeling results emphasize the importance of water transit times
656 within the watershed as a main feature controlling the chemical composition of subsurface
657 waters. Along all the slopes, the waters coming from the vicinity of the crests and
658 characterized by long transit times systematically render higher concentrations than the
659 waters with shorter pathways and transit times. When the hydrological conditions change
660 from wet to dry periods, the solute concentrations also tend to increase with the increase in
661 the mean transit time of waters. Our results show that for the spring and piezometer waters,
662 the spatial and temporal variations of their geochemical composition are fully explained by
663 the differences in water transit times (figure 13). Transit time variations between high and low
664 discharge periods explain the temporal variations of geochemical signatures within each site.
665 Various mean transit times of waters supplying the different sites explain the various chemical
666 compositions between the sites (figure 13). This key role of the water-rock interaction time is
667 in agreement with previous reactive-transport studies conducted in the Strengbach

668 watershed (Ackerer et al., 2018) and in other sites (e.g. Maher, 2010; Moore et al., 2012;
669 Lebedeva and Brantley; 2013).

670 This study also brings new constrains on the spatial distribution of the weathering processes.
671 For the modeling strategy employed, the chemical composition of the spring and piezometer
672 waters are calculated by integrating the chemical composition of waters introduced at
673 different starting locations along the active part of the flow lines (figure 5). The modeling
674 results show that through the geochemical integration, the concentrated waters coming from
675 the main crests are naturally counterbalanced by the diluted waters infiltrating close to the
676 sampling sites. The solute chemistry is acquired through reactions and weathering processes
677 that are spatially relatively homogenous along the flow lines of the watersheds. This spatial
678 homogeneity of the weathering processes helps us to understand why the chemical fluxes
679 carried by the Strengbach stream (Viville et al., 2012), the chemical fluxes from the Strengbach
680 spring waters (Ackerer et al., 2018) and the weathering fluxes locally determined along a
681 regolith profile sampled in the catchment (Ackerer et al., 2016), are all very similar.

682 The modeling also shows that the hydrogeochemical functioning of the watershed is properly
683 simulated by water circulations in the shallow subsurface, i.e., in a saprolitic aquifer. No
684 contribution of waters circulating in the deep fracture network of the granitic bedrock and
685 observed during the drilling campaigns (see Chabaux et al., 2017) is necessary. The deep-water
686 circulations are probably disconnected from the shallow subsurface network, as recently
687 suggested by geochemical studies conducted in the Strengbach watershed (Chabaux et al.,
688 2017; Pierret et al., 2018). This is also in agreement with recent hydrological modeling studies
689 arguing that the catchment behaves like a vertically thin but horizontally wide reservoir (Pan
690 et al., 2015; Weill et al., 2017). The modeling results also show that water in the shallow

691 aquifer flows along streamlines with fairly simple geometries. At the scale of the catchment
692 (figure 4), the geometry of the flow lines validates the hypothesis based on the geochemical
693 and Sr-U isotopic data that the spring waters of these mid-mountain basins are supplied by
694 waters from distinct flow paths without real interconnections (i.e., the Strengbach and
695 Ringelbach watersheds; Schaffhauser et al., 2014; Pierret et al., 2014). Flow paths are
696 therefore distinct along the slopes and occur within the shallow saprolitic aquifer but are not
697 controlled by deep fractures in the bedrock.

698 **6-3 Origins of general chemostatic behavior and of specific C-Q relations**

699 The hydrogeochemical monitoring of the spring, piezometer, and stream waters performed in
700 the Strengbach catchment clearly shows that this catchment has a general chemostatic
701 behavior (e.g., Viville et al., 2012; Ackerer et al., 2018). All the spring and the piezometer
702 waters have chemical concentrations impacted by changes in the hydrological conditions, but
703 the concentration variation ranges are by far narrower than variation ranges of water
704 discharges, which define the chemostatic behavior of a hydrological system. For waters
705 showing the largest concentration variations (spring CS1), there is a modest increase of
706 approximately 10-30% in the concentrations of H_4SiO_4 and Na+ from floods to drought events,
707 while the water discharges may vary by a factor of 15 (figure 8). This modest variability of the
708 solute concentrations over a wide range of water discharges is not specific to the Strengbach
709 catchment; it has been observed in several watersheds spanning different climates and
710 hydrological contexts (Godsey et al., 2009; Clow and Mast, 2010; Kim et al., 2017).

711 Different origins for the chemostatic behavior have been proposed, such as a modification of
712 the mineral reactive surfaces during changing hydrological conditions (Clow and Mast, 2010),
713 a small concentration difference between slow and fast moving waters (Kim et al., 2017), or

714 the fact of reaching an equilibrium concentration along the water pathway (Maher, 2010). The
715 coupled approach NIHM-KIRMAT renews the opportunity to discuss on the origin of the
716 chemostatic behavior in catchments. It is worth noting that the acquisition and the evolution
717 of the water chemistry can be simulated along flow lines that have been determined via timely
718 and spatially distributed hydrological modeling. The strength of this approach is to constrain
719 water transit times independently and before any geochemical simulation.

720 The results from the hydrological model show that the characteristics of the flow lines are
721 affected by the changes in the hydrological conditions (section 4.2). This hydrological
722 functioning implies a covariation between flow velocity and flow length over changing
723 hydrological conditions, with faster flows along longer paths during wet conditions and slower
724 flows along shorter paths during dry periods. This hydrological behavior attenuates the
725 variations of the water transit times over changing hydrological conditions. It also explains
726 why the mean transit times span much narrower variation ranges than the water discharges
727 at the collected springs. For example, the calculated mean transit times of waters for the CS1
728 spring vary from 1.75 to 3.13 months between the strongest flood and the driest period that
729 have been studied, whereas the water discharges vary from 1.523 L/s to 0.098 L/s (figure 8B).
730 Because the time of the water-rock interactions exerts a first-order control on the chemical
731 composition of waters, the weak variability of the mean transit times is directly responsible
732 for the relative stability of the chemical composition of waters within the catchment.

733 In addition to this general chemostatic behavior, each chemical element has a specific
734 response to a change in water transit time as exemplified in figure 9 where are given the
735 concentration-mean transit time relations (C-MTT relations) for H_4SiO_4 and the major cations.
736 In the relevant transit time window for the spring and piezometer waters (figure 9b), the C-

737 MTT relations are linear and C-MTT slopes are significant for H_4SiO_4, modest for Na^+ and weak
738 for Mg^{2+} and K^+ concentrations. The modeling results indicate that the C-MTT slopes are
739 controlled by the competition between primary mineral dissolution and element
740 incorporation into clay minerals. When elemental fluxes from primary mineral dissolution to
741 solution are much higher than fluxes from solution to clay minerals (e.g., H_4SiO_4), the element
742 can accumulate in solution, resulting in a significant C-MTT slope. By contrast, when elemental
743 fluxes from primary mineral dissolution to solution are only slightly higher than fluxes from
744 solution to clay minerals (e.g., K^+), the element accumulates only slowly in solution, resulting
745 in a weak C-MTT slope. Interestingly, when fitting power-laws along C-Q relations ($C=aQ^b$, in
746 caption of figure 8), both 'a' coefficient controlling the height of the C-Q laws and 'b'
747 coefficient controlling the curvature of the C-Q laws are sensitive to the C-MTT slopes (figure
748 9c and 9d). 'a' coefficient is positively corelated with C-MTT slopes while 'b' coefficient is
749 negatively corelated. Solute species with significant C-MTT slopes are more chemodynamic
750 and display higher mean annual concentrations (H_4SiO_4 , $b(H_4SiO_4)=-0.1$, $a(H_4SiO_4)=10^{-4}$),
751 whereas species with weak C-MTT slopes show low mean annual concentrations and are
752 nearly perfectly chemostatic ($a(Mg^{2+})=10^{-5}$, $b(Mg^{2+})=-0.016$, $a(K^+)=10^{-5}$, $b(K^+)=0$, figures 8, 9c
753 and 9d). Our results show that a better knowledge of C-MTT relations is important to explain
754 the contrasted C-Q shapes of chemical elements.

755 It is important to underline that the hydrological modeling with the NIHM code is performed
756 independently and before any geochemical simulations with the KIRMAT code. The fact that
757 the flow rates are well reproduced for all the hydrological contexts between 2010 and 2015
758 supports that the water transit times inferred from the NIHM code are realistic. The fact that
759 the chemical composition of waters is well captured indicates that the combination of the
760 geochemical parameters used in KIRMAT code is able to generate realistic reaction rates, as

761 chemistry is well reproduced while respecting realistic water transit times. No modifications
762 of the reactive surfaces and of the dissolution kinetic constants were necessary to reproduce
763 the seasonal variability of the water chemistry. It is also important to emphasize that the
764 simulated chemical compositions of waters remain far from a state of chemical equilibrium
765 with respect to primary minerals. The calculated Gibbs free energy for the primary minerals
766 ranges from -120 to -100 kJ/mol for apatite, -90 to -80 kJ/mol for biotite and anorthite and -
767 30 to -20 kJ/mol for albite and K-feldspar. These far-from-equilibrium values for the Gibbs free
768 energy imply that the reaction rates calculated using hydrogeochemical codes such as
769 KIRMAT, which are based on the transient state theory (TST, Eyring, 1935; Murphy and
770 Helgeson, 1987), are realistic for most of the primary minerals in this type of hydrological
771 context. Regarding the simulations performed in this study, the relatively short residence
772 times of waters and the precipitation of clay minerals prevent reaching a state of chemical
773 equilibrium between waters and primary minerals at the watershed scale. A water transit time
774 around 8-12 years and a distance as long as 15-20 km would be necessary to reach a chemical
775 equilibrium between water and primary minerals (see Ackerer et al., 2018). This long
776 equilibrium length is explained by the precipitation and the dynamic behavior of clay minerals
777 removing ions from solution and retarding chemical equilibrium with respect to primary
778 minerals. Relying upon a clay solid solution is also appropriate to mimic the clay mineral
779 dynamic in this type of watershed, and a clay mineral assemblage precipitating at
780 thermodynamic equilibrium is able to generate reliable water chemistry (this study) and
781 realistic amount of clay minerals (mass fraction of clay minerals of 2-3 % in the regolith after
782 20 kyr of weathering, more detail in Ackerer et al., 2018).

783 Our results indicate that it is not necessary to mix in different proportions soil and deep waters
784 to generate chemostatic behavior, as proposed by Zhi et al. (2019). Chemostatic behavior can

be generated within a single regolith layer with a homogeneous mineralogy, if as demonstrated, the transit time variability of shallow subsurface waters is dampened by seasonal fluctuations of flow line properties. A large storage of primary minerals and weathering product in the subsurface, as proposed in Musolff et al. (2015), is required but not sufficient to generate chemostatic behavior. Chemostatic behavior also depends on the covariation between flow velocities and flow lengths over changing hydrological conditions. Chemostatic behavior is not explained by a modification of the reactive-surface of minerals in the subsurface (i.e., Clow and Mast, 2010), or by an absence of chemical contrast between slow and rapid flows (i.e., Kim et al., 2017). The precipitation of clay minerals is essential to correctly capture the water chemistry in our study, but the dissolution or redissolution of clays is not a key process to explain chemostatic behavior (i.e., Li et al., 2017). Our study clearly supports the idea defended by Herndon et al. (2018) that a spatial and temporal variability in flow paths is a key process to explain C-Q relations in this type of headwater catchment. Our conclusions can most likely be extended to the other mountainous and relatively steep watersheds of this type, in which water pathways and short transit times are mainly controlled by gravity driven flow along slopes (Weill et al., 2019).

7- Conclusion

This study exemplifies the potential of coupling of low-dimensional and depth-integrated hydrological modeling with hydrogeochemical modeling as a way to better understand variability over time and space of the composition of surface and subsurface waters. The independent estimation of the water transit times provided by hydrological simulations is a clear added value to constrain the geochemical modeling approaches. Our study demonstrates that the seasonal variability of hydraulic conductivities along the slopes is a key process to understand the dynamic of flow lines and the changes of water transit times in the

809 watershed. The variations in flow lines distributions from drought to flood events result in a
810 modest seasonal variability of mean water transit times, which in turn explains the relative
811 stability of the solute concentrations in waters. Our results also show that a better knowledge
812 of the concentration-mean transit time relations (C-MTT relations) is an interesting new step
813 to understand the diversity of C-Q shapes for different chemical elements. The consistency
814 between measured and modeled concentrations while respecting the water-rock interaction
815 times provided by the hydrological simulations shows that it is possible to capture the
816 chemical composition of waters with simply determined reactive surfaces and standard
817 kinetic constants. The results of our simulations strengthen the idea that the low surfaces
818 calculated from the geometrical shapes of minerals are a good estimate of the reactive
819 surfaces in this type of granitic catchment, and certainly the values to be used for
820 hydrogeochemical modeling such as that performed in this work, in addition to the use of the
821 experimental kinetic constants for mineral dissolution.

822

823 **Acknowledgements**: This work and the Julien Ackerer's salary were financially supported by
824 the French ANR Program (Project CANTARE- Alsace) under grant agreement ANR-15-CE06-
825 0014. This work also benefited from fruitful discussions with D. Daval. The authors thank all
826 the reviewers for their constructive comments that improved the quality of the manuscript.

827

Bibliography

Acker, J. G. and Bricker, O. P.: The influence of pH on biotite dissolution and alteration kinetics at low temperature. *Geochim. Cosmochim. Acta*, *56*(8), 3073-3092, 1992.

Ackerer, J., Chabaux, F., Van der Woerd, J., Viville, D., Pelt, E., Kali, E., Lerouge, C., Ackerer, P., Di Chiara Roupert, R. and Négrel, P.: Regolith evolution on the millennial timescale from combined U–Th–Ra isotopes and in situ cosmogenic 10Be analysis in a weathering profile (Strengbach catchment, France). *Earth Planet. Sci. Lett., 453*, 33-43, 2016.

Ackerer, J., Chabaux, F., Lucas, Y., Clément, A., Fritz, B., Beaulieu, E Viville D., Pierret, M.C., Gangloff, S. and Négrel, P.: Monitoring and reactive-transport modeling of the spatial and temporal variations of the Strengbach spring hydrochemistry. *Geochim. Cosmochim. Acta*, *225*, 17-35, 2018.

Ameli, A. A., Beven, K., Erlandsson, M., Creed, I. F., McDonnell, J. J. and Bishop, K.: Primary weathering rates, water transit times, and concentration-discharge relations: A theoretical analysis for the critical zone. *Water Resour. Res.*, *53*, 942-960, 2017.

Amrhein, C. and Suarez, D. L.: Some factors affecting the dissolution kinetics of anorthite at 25 C, *Geochim. Cosmochim. Acta*, *56*, 1815-1826, 1992.

Bao, C., Li, L., Shi, Y., & Duffy, C.: Understanding watershed hydrogeochemistry: 1. Development of RT-Flux-PIHM. *Water Resources Research*, *53*, 2328-2345, 2017.

Beaulieu, E., Goddéris, Y., Donnadieu, Y., Labat, D. and Roelandt, C.: High sensitivity of the continental-weathering carbon dioxide sink to future climate change, *Nature Climate Change*, *2*, 346, 2012.

Beaulieu, E., Lucas, Y., Viville, D., Chabaux, F., Ackerer, P., Goddéris, Y. and Pierret, M. C. : Hydrological and vegetation response to climate change in a forested mountainous catchment, *Modeling Earth Systems and Environment*, *2*, 191, 2016.

Beisman, J. J., Maxwell, R. M., Navarre-Sitchler, A. K., Steefel, C. I., & Molins, S. ParCrunchFlow: an efficient, parallel reactive transport simulation tool for physically and chemically

heterogeneous saturated subsurface environments. *Computational Geosciences*, *19*, 403-422, 2015.

Berger, G., Cadore, E., Schott, J. and Dove, P. M.: Dissolution rate of quartz in lead and sodium electrolyte solutions between 25 and 300 C: Effect of the nature of surface complexes and reaction affinity, *Geochim. Cosmochim. Acta*, *58*, 541-551, 1994.

Brantley, S. L. and Mellott, N. P.: Surface area and porosity of primary silicate minerals, *Am. Mineral.*, *85*, 1767-1783, 2000.

Camporese, M., Paniconi, C., Putti, M. and Orlandini, S.: Surface-subsurface flow modeling with path-based runoff routing, boundary condition-based coupling, and assimilation of multisource observation data, Water Resour. Res. 46, W02512, *doi:10.1029/2008WR007536, 2010.*

Chabaux, F., Viville, D., Lucas, Y., Ackerer, J., Ranchoux, C., Bosia, C, Pierret, M.C., Labasque, T., Aquilina, L., Wyns, R., Lerouge, C., Dezaye, C. and Négrel, P.: Geochemical tracing and modeling of surface and deep water–rock interactions in first-order granitic watersheds (Strengbach and Ringelbach CZOs, France), *Acta Geochim.*, *36*, 363-366, 2017.

Chabaux F., Stille P., Prunier J., Gangloff S., Lemarchand D., Morvan G., Négrel J., Pelt E., Pierret M.C., Rihs S., Schmitt A.D., TrémolièresT., Viville D. Plant-soil-water interactions: Implications from U-Th-Ra isotope analysis in soils, soil solutions and vegetation (Strengbach CZO, France). Geochimica et Cosmochimica Acta, 2019.

Chorover, J., Derry, L. A., & McDowell, W. H.: Concentration-Discharge Relations in the Critical Zone: Implications for Resolving Critical Zone Structure, Function, and Evolution. *Water Resources Research*, *53*, 8654-8659, 2017.

Chou, L., and Wollast, R.: Steady-state kinetics and dissolution mechanisms of albite. *Am. J. Science*, *285*, 963-993, 1985.

Clow, D. W. and Mast, M. A.: Mechanisms for chemostatic behavior in catchments: implications for CO2 consumption by mineral weathering, *Chem. Geol.*, *269*, 40-51, 2010.

878 Diamond, J. S., & Cohen, M. J.: Complex patterns of catchment solute–discharge relationships for
879 coastal plain rivers. *Hydrological processes*, *32*, 388-401. 2018.
880 Daval, D., Calvaruso, C., Guyot, F. and Turpault, M. P.: Time-dependent feldspar dissolution rates
881 resulting from surface passivation: Experimental evidence and geochemical implications. *Earth*
882 *Planet. Sci. Lett.*, *498*, 226-236, 2018.
883 Ebel, B. A. and Loague, K.: Physics-based hydrologic-response simulation: Seeing through the fog of
884 equifinality. *Hydrological Processes: An International Journal*, *20*, 2887-2900, 2006.
885 Eyring, H. The activated complex in chemical reactions. *The Journal of Chemical Physics*, *3*, 107-115,
886 1935.
887 Fichter, J., Turpault, M. P., Dambrine, E. and Ranger, J.: Mineral evolution of acid forest soils in the
888 Strengbach catchment (Vosges mountains, NE France), *Geoderma*, *82*, 315-340, 1998.
889 Fischer, C., Kurganskaya, I., Schäfer, T. and Lüttge, A.: Variability of crystal surface reactivity: What do
890 we know?, *Applied Geochem. 43*, 132-157, 2014.
891 Gangloff, S., Stille, P., Schmitt, A.D. and Chabaux F.: Factors controlling the chemical composition of
892 colloidal and dissolved fractions in soil solutions and the mobility of trace elements in soils,
893 Geochim. Cosmochim. Acta, 189 37–57, 2016.
894 Gangloff, S., Stille, P., Pierret, M. C., Weber, T. and Chabaux, F. : Characterization and evolution of
895 dissolved organic matter in acidic forest soil and its impact on the mobility of major and trace
896 elements (case of the Strengbach watershed), *Geochim. Cosmochim. Acta*, *130*, 21-41, 2014.
897 Gautier, J. M., Oelkers, E. H. and Schott, J.: Are quartz dissolution rates proportional to BET surface
898 areas?, *Geochim. Cosmochim. Acta*, *65*, 1059-1070, 2001.
899 Gérard, F., Clément, A. and Fritz, B.: Numerical validation of a Eulerian hydrochemical code using a 1D
900 multisolute mass transport system involving heterogeneous kinetically controlled reactions, *J.*
901 *Cont. Hydrol.*, *30*, 201-216, 1998.
902 Gh'Mari, E. : *Etude minéralogique, pétrophysique et géochimique de dynamique d'altération d'un*
903 *granite soumis aux dépôts atmosphériques acides (bassin versant du Strengbach, Vosges,*

France). Mécanismes, bilans et modélisation, PhD Thesis,, Université Louis Pasteur, Strasbourg, pp. 200.

Gislason, S. R., Oelkers, E. H., Eiriksdottir, E. S., Kardjilov, M. I., Gisladottir, G., Sigfusson, B., Snorrason, A., Elefsen, S., Hardardottir, J., Torssander, P. and Oskarsson, N.: Direct evidence of the feedback between climate and weathering, *Earth Planet. Sci. Lett.*, *277*, 213-222, 2009.

Goddéris, Y., François, L. M., Probst, A., Schott, J., Moncoulon, D., Labat, D. and Viville, D.: Modelling weathering processes at the catchment scale: the WITCH numerical model, Geochim. Cosmochim. Acta 70, 1128–1147, 2006.

Goddéris, Y., Brantley, S. L., François, L., Schott, J., Pollard, D., Déqué, M. and Dury, M.: Rates of consumption of atmospheric CO_2 through the weathering of loess during the next 100 yr of climate change, *Biogeosciences*, *10*, 135-148, 2013.

Godsey, S. E., Kirchner, J. W., and Clow, D. W.: Concentration–discharge relationships reflect chemostatic characteristics of US catchments. *Hydrological Processes: An International Journal*, *23*, 1844-1864, 2009.

Guidry, M. W. and Mackenzie, F. T.: Experimental study of igneous and sedimentary apatite dissolution: control of pH, distance from equilibrium, and temperature on dissolution rates, *Geochim. Cosmochim. Acta*, *67*, 2949-2963, 2003.

Gunduz, O. and Aral, M. M.: River networks and groundwater flow: a simultaneous solution of a coupled system, *J. Hydrol.*, *301*, 216-234, 2005.

Gupta, H.V., Kling, H., Yilmaz, K.K., Martinez, G.F. Decomposition of the mean squared error and NSE performance criteria: Implications for improving hydrological modelling. J. Hydrol. 377, 80–91, 2009.

Hazenberg, P., Broxton, P., Gochis, D., Niu, G. Y., Pangle, L. A., Pelletier, J. D., ... and Zeng, X. (2016). Testing the hybrid-3-D hillslope hydrological model in a controlled environment, *Wat. Resour. Res.*, *52*, 1089-1107, 2016.

929 Herndon, E. M., Steinhoefel, G., Dere, A. L., & Sullivan, P. L.: Perennial flow through convergent
930 hillslopes explains chemodynamic solute behavior in a shale headwater catchment. *Chemical*
931 *Geology*, *493*, 413-425, 2018.
932 Jeannot, B., Weill, S., Eschbach, D., Schmitt, L. and Delay, F.: A low-dimensional integrated subsurface
933 hydrological model coupled with 2-D overland flow: Application to a restored fluvial
934 hydrosystem (Upper Rhine River–France), J. Hydrol., 563, 495-509, 2018.
935 Kampf, S. K. and Burges, S. J.: A framework for classifying and comparing distributed hillslope and
936 catchment hydrologic models, *Water Resour. Res.*, W05423, doi:10.1029/2006WR005370,
937 2007
938 Kim, H., Dietrich, W. E., Thurnhoffer, B. M., Bishop, J. K. and Fung, I. Y.: Controls on solute
939 concentration-discharge relationships revealed by simultaneous hydrochemistry observations
940 of hillslope runoff and stream flow: The importance of critical zone structure, *Water Resour.*
941 *Res.*, *53*, 1424-1443, 2017.
942 Kirchner, J. W.: Getting the right answers for the right reasons: Linking measurements, analyses, and
943 models to advance the science of hydrology, *Water Resour. Res. 42,* W03S04,
944 doi:10.1029/2005WR004362, 2006.
945 Lebedeva, M. I. and Brantley, S. L. : Exploring geochemical controls on weathering and erosion of
946 convex hillslopes: Beyond the empirical regolith production function. *Earth Surface Processes*
947 *and Landforms*, *38*, 1793-1807, 2013.
948 Li, D. D., Jacobson, A. D. and McInerney, D. J.: A reactive-transport model for examining tectonic and
949 climatic controls on chemical weathering and atmospheric CO2 consumption in granitic
950 regolith. *Chem. Geol.*, *365*, 30-42 2014.
951 Li, L., Peters, C. A. and Celia, M. A.: Upscaling geochemical reaction rates using pore-scale network
952 modeling. *Advances in water resources*, *29*, 1351-1370, 2006.

953 Li, L., Bao, C., Sullivan, P. L., Brantley, S., Shi, Y., & Duffy, C. Understanding watershed
954 hydrogeochemistry: 2. Synchronized hydrological and geochemical processes drive stream
955 chemostatic behavior. *Water Resources Research*, *53*, 2346-2367, 2017.
956 Li, L., Maher, K., Navarre-Sitchler, A., Druhan, J., Meile, C., Lawrence, C., ... and Jin, L. : Expanding the
957 role of reactive transport models in critical zone processes. *Earth-Science Reviews*, *165*, 280-
958 301, 2017

959 Lucas, Y., Schmitt, A. D., Chabaux, F., Clément, A., Fritz, B., Elsass, P. and Durand, S.: Geochemical
960 tracing and hydrogeochemical modelling of water–rock interactions during salinization of
961 alluvial groundwater (Upper Rhine Valley, France), *Appl. Geochem.*, *25*, 1644-1663, 2010.

962 Lucas, Y., Chabaux, F., Schaffhauser, T., Fritz, B., Ambroise, B., Ackerer, J. and Clément, A.:
963 Hydrogeochemical modeling (KIRMAT) of spring and deep borehole water compositions in the
964 small granitic Ringelbach catchment (Vosges Mountains, France), *Applied Geochemistry*, *87*, 1-
965 21, 2017.
966 Lundström, U. and Öhman, L. O.: Dissolution of feldspars in the presence of natural, organic solutes,
967 *Journal of Soil Science*, *41*, 359-369, 1990.
968 Maher, K., Steefel, C. I., White, A. F., & Stonestrom, D. A.: The role of reaction affinity and secondary
969 minerals in regulating chemical weathering rates at the Santa Cruz Soil Chronosequence,
970 California, *Geochim. Cosmochim. Acta*, *73*, 2804-2831, 2009.
971 Maher, K. : The dependence of chemical weathering rates on fluid residence time, *Earth Planet. Sci.*
972 *Lett.*, *294*, 101-110, 2010.
973 Maher, K.: The role of fluid residence time and topographic scales in determining chemical fluxes from
974 landscapes, *Earth Planet. Sci. Let.*, *312*, 48-58, 2011.

975 Mirus, B. B., Ebel, B. A., Heppner, C. S. and Loague, K.: Assessing the detail needed to capture rainfall-
976 runoff dynamics with physics-based hydrologic response simulation, *Water Resour. Res.*, *47*,
977 W00H10, doi:10.1029/2010WR009906, 2011

978 Moore, J., Lichtner, P. C., White, A. F. and Brantley, S. L.: Using a reactive transport model to elucidate
979 differences between laboratory and field dissolution rates in regolith, *Geochim. Cosmochim.*
980 *Acta*, *93*, 235-261, 2012.

981 Murphy, W. M., & Helgeson, H. C. Thermodynamic and kinetic constraints on reaction rates among
982 minerals and aqueous solutions. III. Activated complexes and the pH-dependence of the rates
983 of feldspar, pyroxene, wollastonite, and olivine hydrolysis. *Geochimica et Cosmochimica Acta*,
984 *51*, 3137-3153, 1987.

985 Nagy. K. L.. White. A. F.. & Brantley. S. L. Chemical weathering rates of silicate minerals. *Mineralogical*
986 *Society of America. Washington. DC*. 1995.

987 Navarre-Sitchler, A. and Brantley, S.: Basalt weathering across scales, *Earth and Planet. Sci. Let.*, *261*,
988 321-334, 2007.

989 Navarre-Sitchler, A., Steefel, C. I., Yang, L., Tomutsa, L. and Brantley, S. L.: Evolution of porosity and
990 diffusivity associated with chemical weathering of a basalt clast, *Journal of Geophysical*
991 *Research: Earth Surface*, *114*, F02016, doi:10.1029/2008JF001060, 2009.

992 Ngo, V. V., Delalande, M., Clément, A., Michau, N. and Fritz, B.: Coupled transport-reaction modeling
993 of the long-term interaction between iron, bentonite and Callovo-Oxfordian claystone in
994 radioactive waste confinement systems., *Applied Clay Science*, *101*, 430-443, 2014

995 Pan, Y., Weill, S., Ackerer, P. and Delay, F.: A coupled stream flow and depth-integrated subsurface
996 flow model for catchment hydrology, *Journal of Hydrology*, *530*, 66-78, 2015

997 Pierret, M. C., Cotel, S., Ackerer, P., Beaulieu, E., Benarioumlil, S., Boucher, M., ... & Friedmann, P.:
998 The Strengbach catchment: A multidisciplinary environmental sentry for 30 years. *Vadose*
999 *Zone Journal*, *17*, 2018.

1000 Pierret, M. C., Stille, P., Prunier, J., Viville, D., & Chabaux, F. Chemical and U–Sr isotopic variations in
1001 stream and source waters of the Strengbach watershed (Vosges mountains, France).
1002 *Hydrology and Earth System Sciences*, *18*, 2014.

1003 Pollet-Villard, M., Daval, D., Ackerer, P., Saldi, G. D., Wild, B., Knauss, K. G. and Fritz, B.: Does
1004 crystallographic anisotropy prevent the conventional treatment of aqueous mineral reactivity?
1005 A case study based on K-feldspar dissolution kinetics, *Geochim. Cosmochim. Acta*, *190*, 294-
1006 308, 2016.

1007 Prunier, J., Chabaux, F., Stille, P., Gangloff, S., Pierret, M. C., Viville, D. and Aubert, A. : Geochemical
1008 and isotopic (Sr, U) monitoring of soil solutions from the Strengbach catchment (Vosges
1009 mountains, France): Evidence for recent weathering evolution, *Chem. Geol.*, *417*, 289-305,
1010 2015.

1011 Schaffhauser, T., Chabaux, F., Ambroise, B., Lucas, Y., Stille, P., Reuschlé, T., Perrone, T. and Fritz, B.:
1012 Geochemical and isotopic (U, Sr) tracing of water pathways in the granitic Ringelbach
1013 catchment (Vosges Mountains, France), *Chem. Geol.*, *374*, 117-127, 2014.

1014 Schmitt, A.D., Gangloff, S., Labolle, F., Chabaux, F. and Stille, P.: Ca biogeochemical cycle at the beech
1015 tree - soil solution interface from the Strengbach CZO (NE France): insights from stable Ca and
1016 radiogenic Sr isotopes, Geochim. and Cosmochim. Acta 213, 91-109, 2017

1017 Schmitt AD, Borrelli N., Ertlen D., Gangloff S., Chabaux, F. and Osterrieth M.: Stable calcium isotope
1018 speciation and calcium oxalate production within beech tree (Fagus sylvatica L.) organs,
1019 Biogeochemistry, 137,197-217, DOI 10.1007/s10533-017-0411-0, 2018.

1020 Steefel, C. I., DePaolo, D. J. and Lichtner, P. C.: Reactive transport modeling: An essential tool and a
1021 new research approach for the Earth sciences, *Earth Planet. Sci. Let.*, *240*, 539-558, 2005

1022 Tardy, Y. and Fritz, B.: An ideal solid solution model for calculating solubility of clay minerals, *Clay*
1023 *minerals*, *16*, 361-373, 1981.

1024 Viville, D., Chabaux, F., Stille, P., Pierret, M. C. and Gangloff, S.: Erosion and weathering fluxes in granitic
1025 basins: the example of the Strengbach catchment (Vosges massif, eastern France), *Catena*, *92*,
1026 122-129, 2012.

Weill, S., Altissimo, M., Cassiani, G., Deiana, R., Marani, M. and Putti, M.: Saturated area dynamics and streamflow generation from coupled surface–subsurface simulations and field observations, *Advances in water resources*, *59*, 196-208, 2013.

Weill, S., Delay, F., Pan, Y. and Ackerer, P.: A low-dimensional subsurface model for saturated and unsaturated flow processes: ability to address heterogeneity, *Computational Geosciences*, *21*, 301-314, 2017.

Weill, S., Lesparre, N., Jeannot, B., & Delay, F. Variability of Water Transit Time Distributions at the Strengbach Catchment (Vosges Mountains, France) Inferred Through Integrated Hydrological Modeling and Particle Tracking Algorithms. *Water*, 2637, 2019.

White, A. F. and Brantley, S. L.: The effect of time on the weathering of silicate minerals: why do weathering rates differ in the laboratory and field?, *Chem. Geol.*, *202*, 479-506, 2003.

Wild, B., Daval, D., Guyot, F., Knauss, K. G., Pollet-Villard, M. and Imfeld, G.: pH-dependent control of feldspar dissolution rate by altered surface layers, *Chemical Geology*, *442*, 148-159, 2016.

Zhi, W., Li, L., Dong, W., Brown, W., Kaye, J., Steefel, C., & Williams, K. H. Distinct Source Water Chemistry Shapes Contrasting Concentration-Discharge Patterns. *Water Resources Research*. 2019.

Zhu, C.: In situ feldspar dissolution rates in an aquifer, *Geochim. Cosmochim. Acta*, *69*, 1435-1453, 2005.

Figure and table captions

Figure 1: sampling locations within the Strengbach catchment. Blue stars represent springs, blue diamonds represent piezometers, and the blue circle represents the stream at the outlet of the watershed. Green circles represent soil solution locations, and black diamonds represent bedrock facies locations.

Figure 2: on the left: calibrated field of thicknesses of the weathered material constituting the shallow unconfined aquifer at the Strengbach catchment used for the simulations by NIHM. The 1D surface draining network used in NIHM is represented by the black lines. The mesh for the groundwater compartment is represented by grey lines. On the right: fitting observed flow rates from the Strengbach stream at the outlet of the catchment with simulations of flow within the watershed (illustrated from 2010 to 2015). The subsurface compartment inherits from the aquifer thicknesses reported in the left panel, and the topography lets the natural outlet of the subsurface compartment being the surface draining network.

Figure 3: principle of the method of backtracking used to determine flow lines that generate flow at the outlet of the Strengbach catchment. Particles are dispatched along the wet fraction of the 1D river network (only one is represented here at a position *a* on 01/01/2010 at 23:59). NIHM generates an output heterogeneous velocity field at that date for the whole watershed, denoted $V_{01/01/2010}$. By using a velocity field of the same magnitude but opposite direction to the particle, the position of the particle is backtracked until 31/12/2009 23:59. Then, to further backtrack the trajectory of the particle, the velocity field is updated accordingly. The frequency of velocity field updates is set to one day.

Figure 4: at the top, flow lines of the subsurface that feed with water the surface draining network on March 1st, 2010 (on the left, high-flow period) and July 1st, 2010 (on the right, low-flow period). The color scale indicates that a water particle reaching the river at a given date started its travel along the streamline or passed at a given location on the streamline x days prior. The density of streamlines is associated with the flowing versus dry fraction of the river network at a prescribed date. Below, flow lines of the subsurface that feed with water the geochemical sampling sites on March 30th, 2010 (on the left, flood event) and November 29th, 2011 (right, drought event) according to NIHM simulations. For each sampling site, 10 particles were dispatched in the direct neighborhood of the site and then backtracked to render 10 stream lines. The color scale for times is similar to that of the top plot.

Figure 5: conceptual scheme used in the modeling of the water chemistry. The soil solutions are used as input solution. Cells represent the grid of the reactive-transport code KIRMAT. The regolith is discretized into a 1D succession of cells along the active parts of the flow lines determined by the NIHM hydrological model. The hydrogeochemical model KIRMAT evaluates transport and geochemical processes within each cell. The integrated chemistry of sampled waters is the arithmetic mean of solute concentrations with regularly distributed inlet points along a stream line.

Figure 6: maps of piezometric gradient and depth-integrated hydraulic conductivity for the Strengbach catchment, as simulated by NIHM, on 29/11/2011 (dry period) and 30/03/2010 (high flows period). The mean hydraulic conductivity is integrated normal to bedrock of the aquifer and thus depends on the water saturation of the vadose zone and the location of the water table.

Figure 7: simulation results for the CS1 spring for an important drought (29/11/2011) and a strong flood event (30/03/2010). At the top, active parts of the flow lines bringing the waters to the CS1 spring for the two sampling dates (7A and7B). Below, simulated chemical compositions of CS1 spring waters after integration along the flow lines and comparison with the initial soil solution and the spring chemistry data (7C and7D). Error bars show analytical uncertainties on measured concentrations and induced uncertainties in model results (the propagation in the KIRMAT simulations of analytical uncertainties from pH and chemical concentrations measured in the soil solutions).

Figure 8: simulation results for the CS1 spring over the whole range of the water discharges from the spring. Results are presented for H_4SiO_4, Na^+, K^+ and Mg^{2+} concentrations (8A, 8C, 8E and 8F), pH (8D) and mean water transit time (8B). Red lines indicate simulated parameters after integration along the flow lines, and blue points show measured values collected between 2005 and 2015. Corresponding dates and data for the modeled samples are given in table 1. The overall geochemical database is available in supplementary table EA1. Error bars show analytical uncertainties on measured concentrations and induced uncertainties in model results (the propagation in the KIRMAT simulations of analytical uncertainties from pH and chemical concentrations measured in the soil solutions). Fitting a power law of type $C=a*Q^b$ along the C-Q relations gives the following parameters: $a(H_4SiO_4)=10^{-4}$, $b(H_4SiO_4)=-0.1$; $a(Na^+)=7\times10^{-5}$, $b(Na^+)=-0.053$; $a(Mg^{2+})=10^{-5}$, $b(Mg^{2+})=-0.016$; $a(K^+)=10^{-5}$, $b(K^+)=0$.

Figure 9: (9A) evolution of solute concentrations for H_4SiO_4, Na^+, K^+, Mg^{2+} and Ca^{2+} as a function of mean water transit time in the Strengbach watershed. Water transit times are between 1.75 and 4 months for all the springs and piezometers in this study. (9B) Focus on the transit time window (1.75-4 months) for the studied waters and equations linking mean water transit

1114 times and concentrations for H_4SiO_4, Na^+, K^+, Mg^{2+} and Ca^{2+}. Relations between transit times
1115 and concentrations are linear within this window (9C) relations between 'b' coefficients
1116 ($C=a*Q^b$) and the concentration-transit time slopes for the chemical elements. (9D) relations
1117 between 'a' coefficients ($C=a*Q^b$) and the concentration-transit time slopes for the chemical
1118 elements. Elements with significant concentration-mean transit time slopes are slightly
1119 chemodynamic (e.g. H_4SiO_4 and Na^+), while elements with low concentration-mean transit
1120 time slopes are almost chemostatic in the watershed (e.g. K^+ and Mg^{2+}). Ca^{2+} is not shown on
1121 9C and 9D figures as this element is affected by a strong multi-annual concentration decrease
1122 that prevents a meaningful C-Q power law analysis (Ackerer et al., 2018).

1123 Figure 10: simulation results for the PZ3 and PZ5 piezometers for a flood event (05/05/2015).
1124 At the top, active parts of the flow lines that bring waters to the two sampling sites (10A and
1125 10B). Below, simulated chemical compositions of the piezometer waters after integration
1126 along the flow lines and comparison with the initial soil solution and the water chemistry data
1127 (10C and 10D). Error bars show analytical uncertainties on measured concentrations and
1128 induced uncertainties in model results (the propagation in the KIRMAT simulations of
1129 analytical uncertainties from pH and chemical concentrations measured in the soil solutions).

1130 Figure 11: simulation results for the CS2 spring. At the top, active parts of the flow lines that
1131 bring water to the CS2 spring for drought (29/11/2011) and flood (30/03/2010) events (11A
1132 and 11B). The CS2 location results in more scattered flow lines than for CS1 spring. Below,
1133 simulation results for the CS2 spring over the whole range of experienced discharges (11C and
1134 11D). Blue lines indicate simulated parameters after integration along the slowest flow line,
1135 yellow lines indicate simulated parameters after integration along the fastest flow line, and
1136 blue points show measured values collected between 2005 and 2015 (data in table 1 and in

supplementary table EA2). Error bars show analytical uncertainties on measured concentrations and induced uncertainties in model results (the propagation in the KIRMAT simulations of analytical uncertainties from pH and chemical concentrations measured in the soil solutions).

Figure 12: simulation results for the RH3 spring chemistry and for a flood event (30/03/2010). Left, simulated concentrations by assuming flow lines running through gneiss (GN) only (12A). Right, simulated concentrations by assuming flow lines running through hydrothermally altered granite (VS) only (12B). Error bars show analytical uncertainties on measured concentrations and induced uncertainties in model results (the propagation in the KIRMAT simulations of analytical uncertainties from pH and chemical concentrations measured in the soil solutions).

Figure 13: overview of the simulated flow lines in the subsurface that feed with water the geochemical sampling sites CS1, PZ3, and PZ5 on May 5th, 2015. The simulated chemical compositions after geochemical integration along the flow lines are compared with the initial soil solution and the spring chemistry data.

Table 1: measured pH, water discharges and chemical concentrations of H_4SiO_4, Na^+, K^+, Mg^{2+}, and Ca^{2+} in water samples collected at the Strengbach catchment and used for the hydrogeochemical modeling. The sampling sites include springs (CS1, CS2, RH3) and piezometers (PZ3, PZ5).

Table 2: Initial and calibrated values of the hydrodynamic parameters of the aquifer in the hydrological simulation of the Strengbach catchment by NIHM.

Table 3: Comparison between BET surfaces and geometric surfaces for the major primary minerals present in a granitic context. BET surfaces were measured via gas absorption

experiments by [1] Berger et al., 1994; [2] Chou and Wollast, 1985; [3] Lundstrom and Ohman, 1990; [4] Amrhein and Suarez, 1992; [5] Acker and Bricker, 1992; and [6] Guidry and Mackenzie, 2003. Geometric surfaces were recalculated from the granulometric ranges of the minerals and by assuming a spherical geometry.

	Na^+ (mmol/L)	K^+ (mmol/L)	Mg^{2+} (mmol/L)	Ca^{2+} (mmol/L)	H_4SiO_4 (mmol/L)	pH	Water Discharge (L/s)
Spring CS1							
16/09/2008	0.071	0.013	0.017	0.044	0.129	6.28	0.954
30/03/2010	0.074	0.014	0.015	0.043	0.120	5.61	1.523
29/03/2011	0.074	0.013	0.015	0.038	0.145	6.23	0.345
04/10/2011	0.080	0.012	0.016	0.042	0.176	6.57	0.122
29/11/2011	0.088	0.015	0.019	0.034	0.177	6.30	0.098
05/05/2015	0.065	0.012	0.012	0.054	0.121	5.33	1.410
Spring CS2							
30/03/2010	0.090	0.020	0.020	0.080	0.122	6.15	6.274
29/03/2011	0.090	0.020	0.020	0.070	0.144	6.18	0.956
02/08/2011	0.090	0.020	0.020	0.060	0.170	6.50	2.171
04/10/2011	0.100	0.020	0.020	0.070	0.177	6.76	0.413
29/11/2011	0.100	0.020	0.020	0.060	0.180	6.22	0.285
05/05/2015	0.077	0.016	0.018	0.074	0.123	6.14	7.500
Spring RH3							
30/03/2010	0.083	0.028	0.032	0.081	0.127	6.28	-
Piezometer PZ3							
05/05/2015	0.074	0.013	0.011	0.053	0.153	6.29	-
Piezometer PZ5							
05/05/2015	0.072	0.013	0.017	0.058	0.132	6.16	-

Table 1

Parameter	Unit	Initial Value	Calibrated value
Depth of substratum	m	4	See figure 2
Saturated hydraulic conductivity (all zones except the low depth zone at the catchment peak (see figure 2))	$m.s^{-1}$	1E-04	8E-05
Saturated hydraulic conductivity (catchment peak)	$m.s^{-1}$	1E-04	1E-04
porosity (all zones except the low depth zone at the catchment peak)	-	0.1	0.08
Porosity (catchment peak)	-	0.1	0.2
Residual water content (all zones)	-	0.01	0.01
Specific storage (all zones)	m^{-1}	1E-08	1E-08
n (Van Genuchten coefficient, all zones)	-	2	2
α (Van Genuchten coefficient, all zones)	m^{-1}	1	1.5
Thickness of the interface layer between the groundwater compartment and the surface compartment	m	0.1	0.05
Saturated hydraulic conductivity of the interface layer between the groundwater compartment and the surface compartment	$m.s^{-1}$	1E-04	1.2E-05

Table 2

Mineral	**Mineral density** (g/cm^3)	**Granulometric range** (μm)	**Particle radius** (μm)	**Spherical geometric surface** (m^2/g)	**BET surface** (m^2/g)
Quartz[1]	2.62	< 50	1 - 25	1.150 - 0.046	0.310
Albite[2]	2.60	50 - 100	25 - 50	0.046 - 0.023	0.075
K-feldspar[3]	2.56	< 50	1 - 25	1.170 - 0.047	1.420
Anorthite[4]	2.73	20 - 50	10 - 25	0.044 - 0.111	0.500
Biotite[5]	3.09	150 - 400	75 - 200	0.013 - 0.005	0.240
Apatite[6]	3.19	100 - 200	50 - 100	0.018 – 0.009	0.026

Table 3

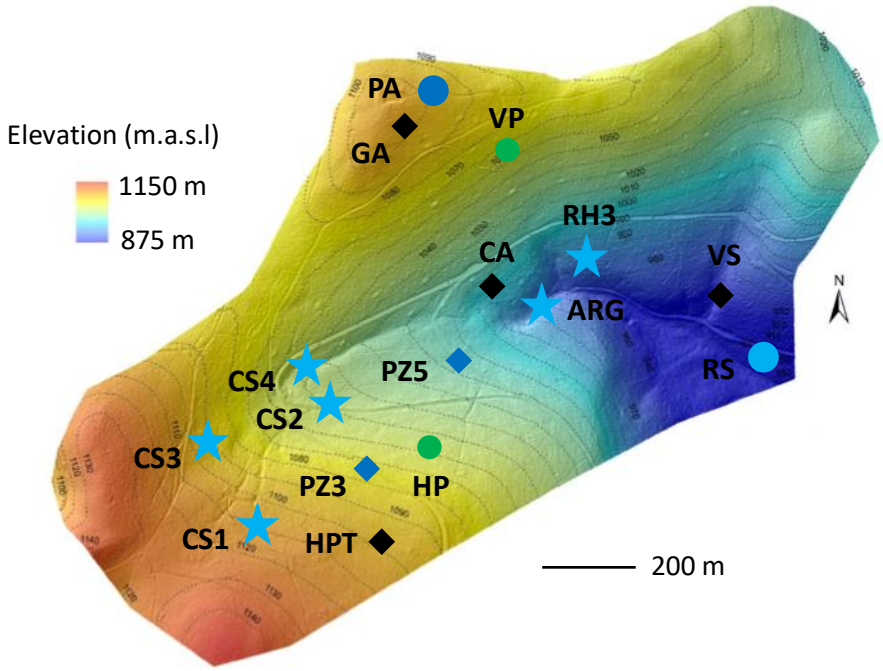
Elevation (m.a.s.l)
1150 m
875 m
PA
VP
GA
RH3
CA
VS
ARG
RS
PZ5
CS4
CS2
CS3
PZ3
HP
CS1
HPT
200 m
N

Figure 1

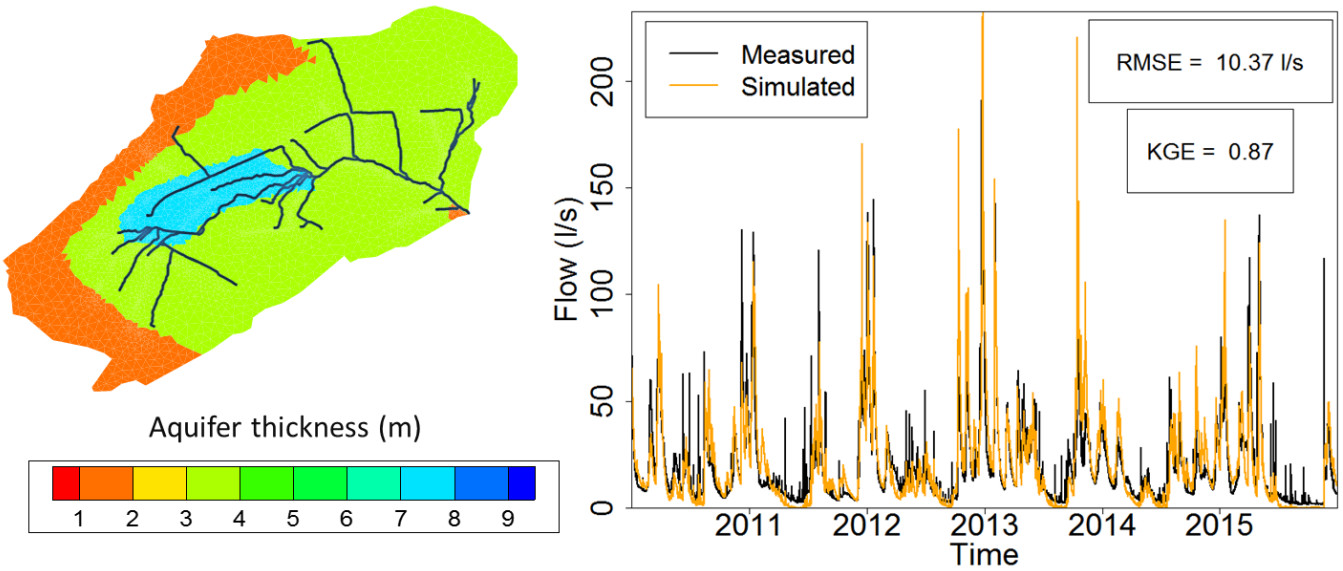
Aquifer thickness (m)
1
2
3
4
5
6
7
8
9
Measured
Simulated
RMSE = 10.37 l/s
KGE = 0.87
Flow (l/s)
0
50
100
150
200
2011
2012
2013
2014
2015
Time

Figure 2

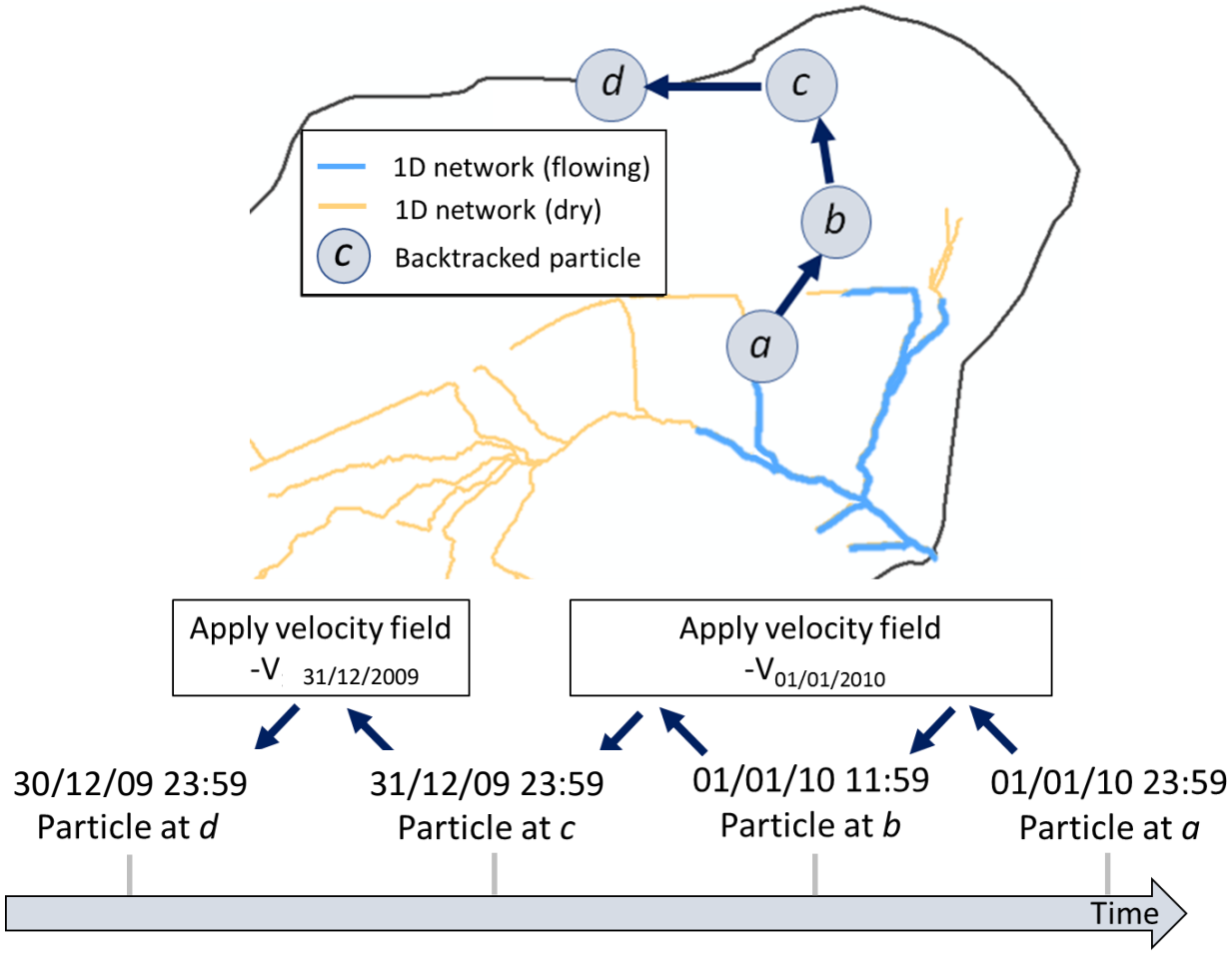
d
c
b
a
1D network (flowing)
1D network (dry)
c
Backtracked particle
Apply velocity field
-V 31/12/2009
Apply velocity field
-V01/01/2010
30/12/09 23:59
Particle at d
31/12/09 23:59
Particle at c
01/01/10 11:59
Particle at b
01/01/10 23:59
Particle at a
Time

Figure 3

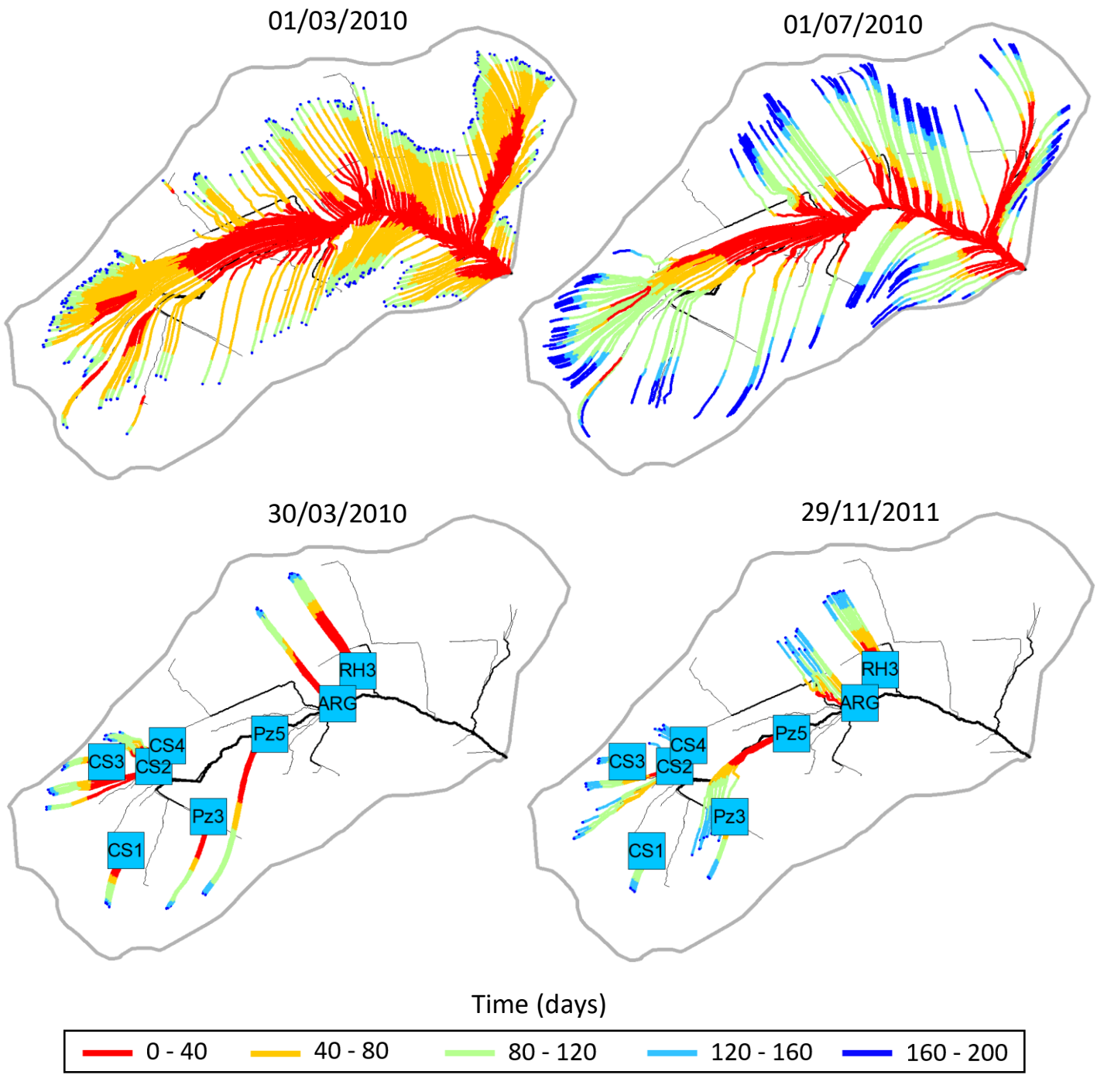
01/03/2010
01/07/2010
30/03/2010
29/11/2011
RH3
ARG
Pz5
CS4
CS3
CS2
Pz3
CS1
Time (days)
0 - 40
40 - 80
80 - 120
120 - 160
160 - 200

Figure 4

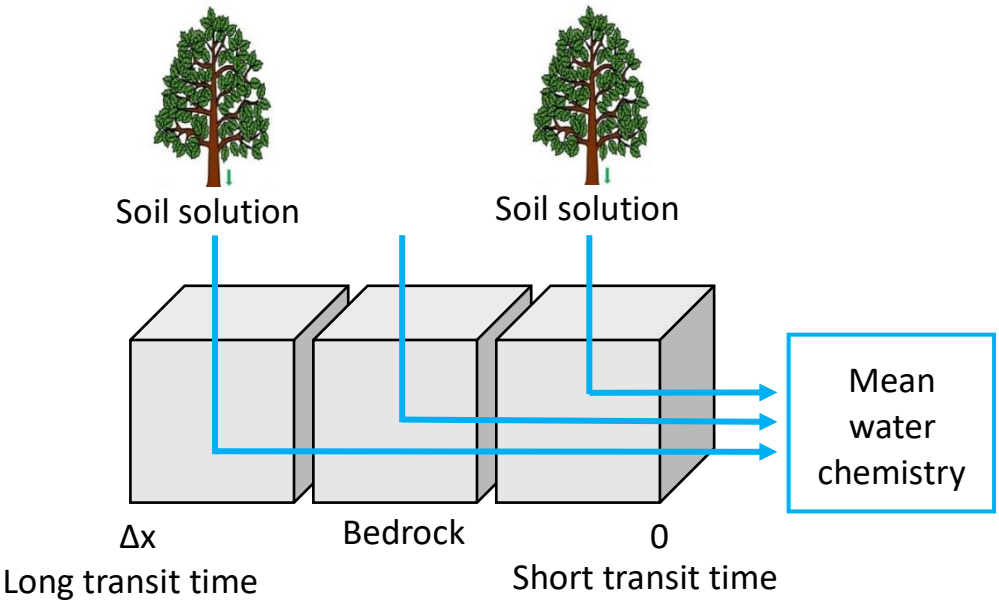
Soil solution
Soil solution
Mean
water
chemistry
Δx
Long transit time
Bedrock
0
Short transit time

Figure 5

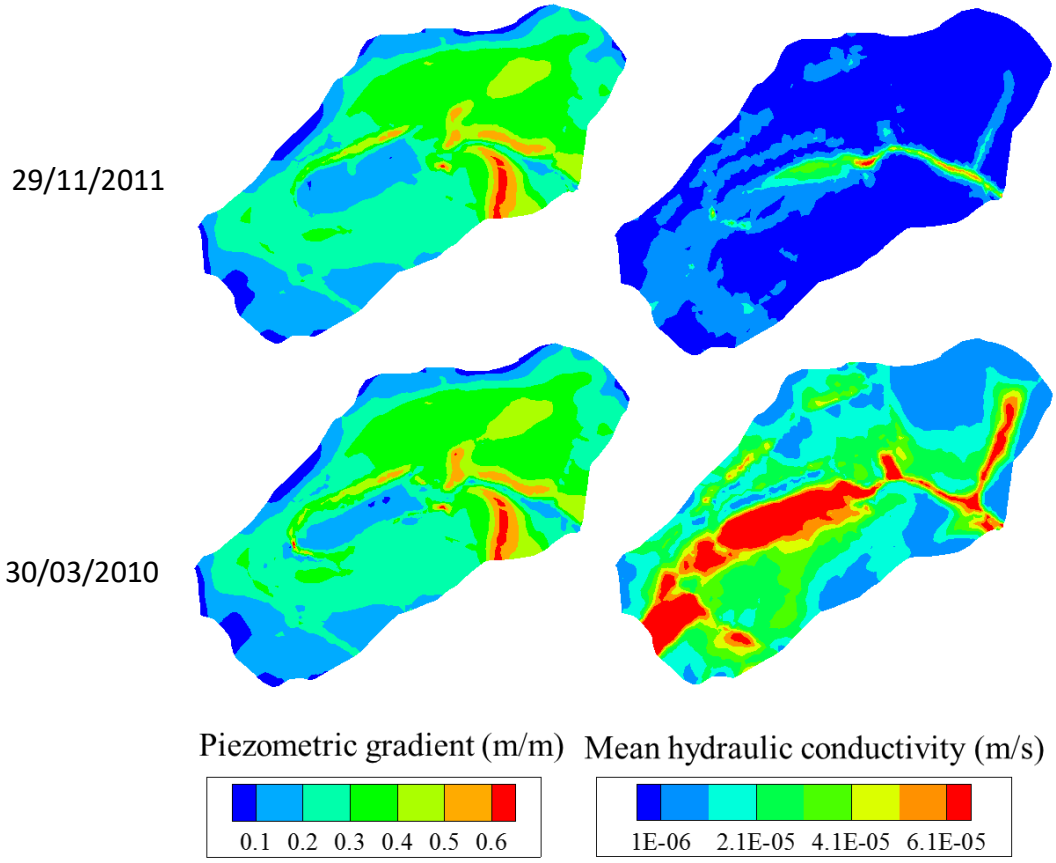
29/11/2011
30/03/2010
Piezometric gradient (m/m)
0.1 0.2 0.3 0.4 0.5 0.6
Mean hydraulic conductivity (m/s)
1E-06 2.1E-05 4.1E-05 6.1E-05

Figure 6

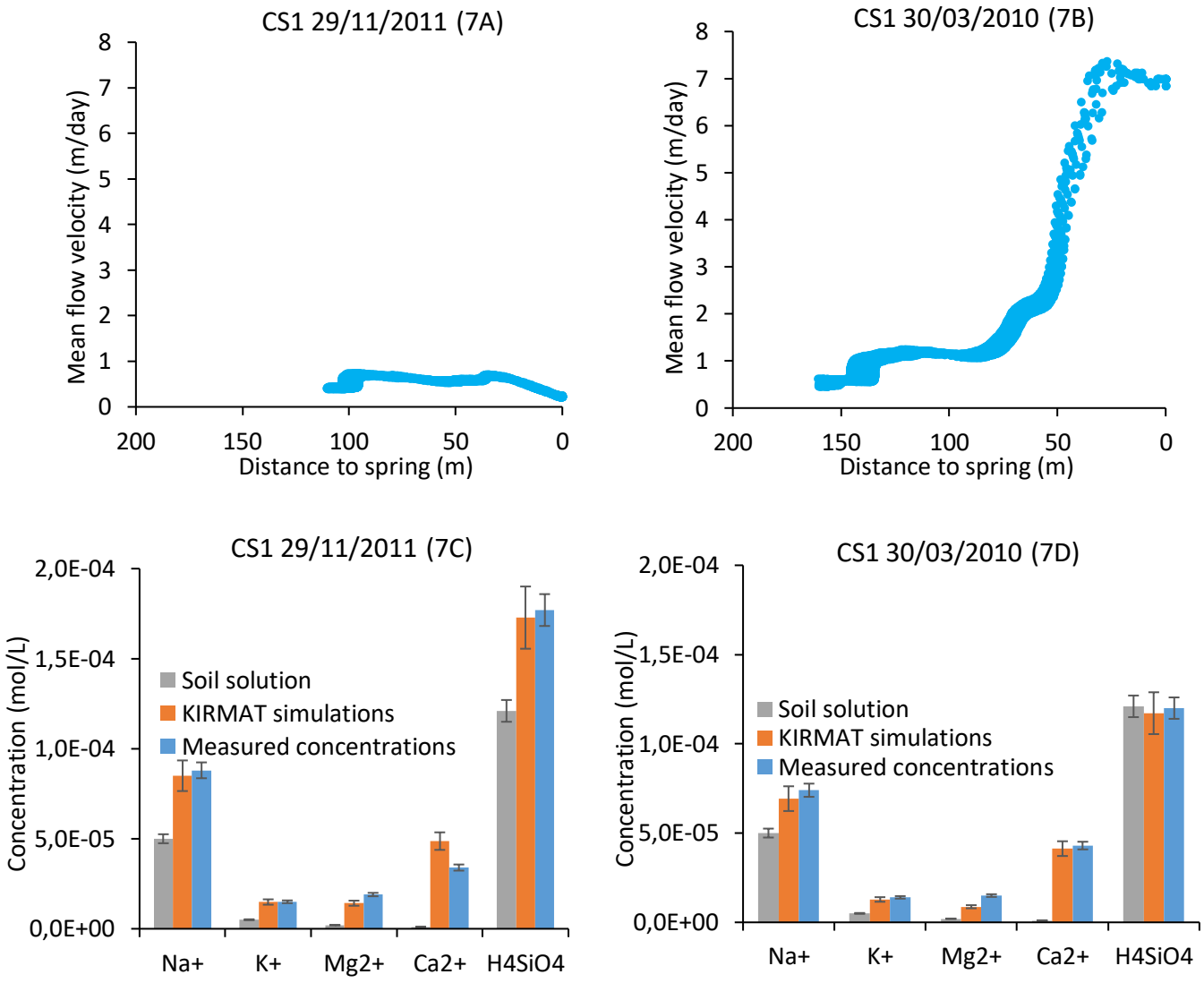
CS1 29/11/2011 (7A)
Mean flow velocity (m/day)
Distance to spring (m)
CS1 30/03/2010 (7B)
Mean flow velocity (m/day)
Distance to spring (m)
CS1 29/11/2011 (7C)
Concentration (mol/L)
Soil solution
KIRMAT simulations
Measured concentrations
Na+
K+
Mg2+
Ca2+
H4SiO4
CS1 30/03/2010 (7D)
Concentration (mol/L)
Soil solution
KIRMAT simulations
Measured concentrations
Na+
K+
Mg2+
Ca2+
H4SiO4

Figure 7

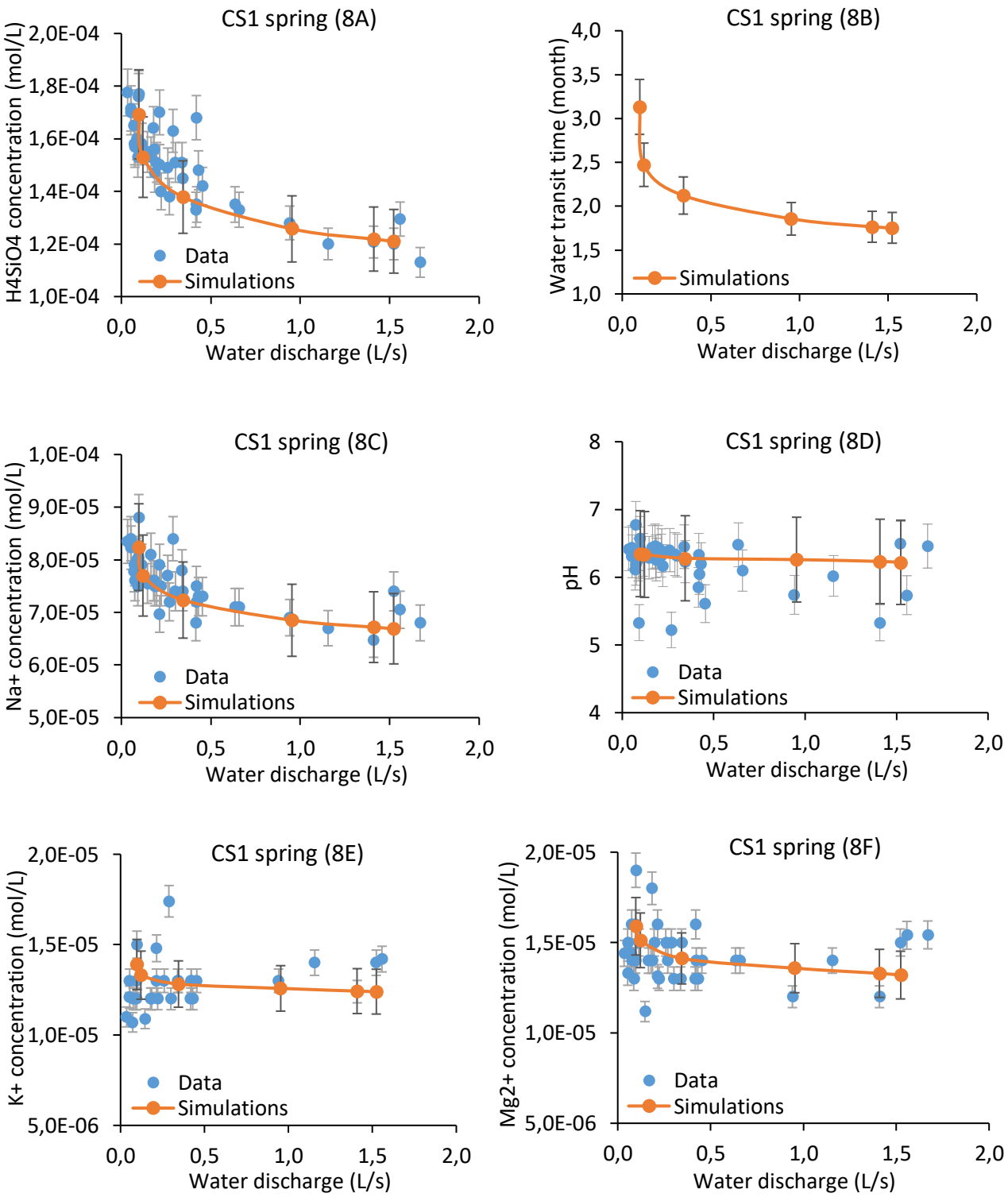
CS1 spring (8A)
H4SiO4 concentration (mol/L)
2,0E-04
1,8E-04
1,6E-04
1,4E-04
1,2E-04
1,0E-04
Data
Simulations
0,0
0,5
1,0
1,5
2,0
Water discharge (L/s)
CS1 spring (8B)
Water transit time (month)
4,0
3,5
3,0
2,5
2,0
1,5
1,0
Simulations
Water discharge (L/s)
CS1 spring (8C)
Na+ concentration (mol/L)
1,0E-04
9,0E-05
8,0E-05
7,0E-05
6,0E-05
5,0E-05
Data
Simulations
Water discharge (L/s)
CS1 spring (8D)
pH
8
7
6
5
4
Data
Simulations
Water discharge (L/s)
CS1 spring (8E)
K+ concentration (mol/L)
2,0E-05
1,5E-05
1,0E-05
5,0E-06
Data
Simulations
Water discharge (L/s)
CS1 spring (8F)
Mg2+ concentration (mol/L)
2,0E-05
1,5E-05
1,0E-05
5,0E-06
Data
Simulations
Water discharge (L/s)

Figure 8

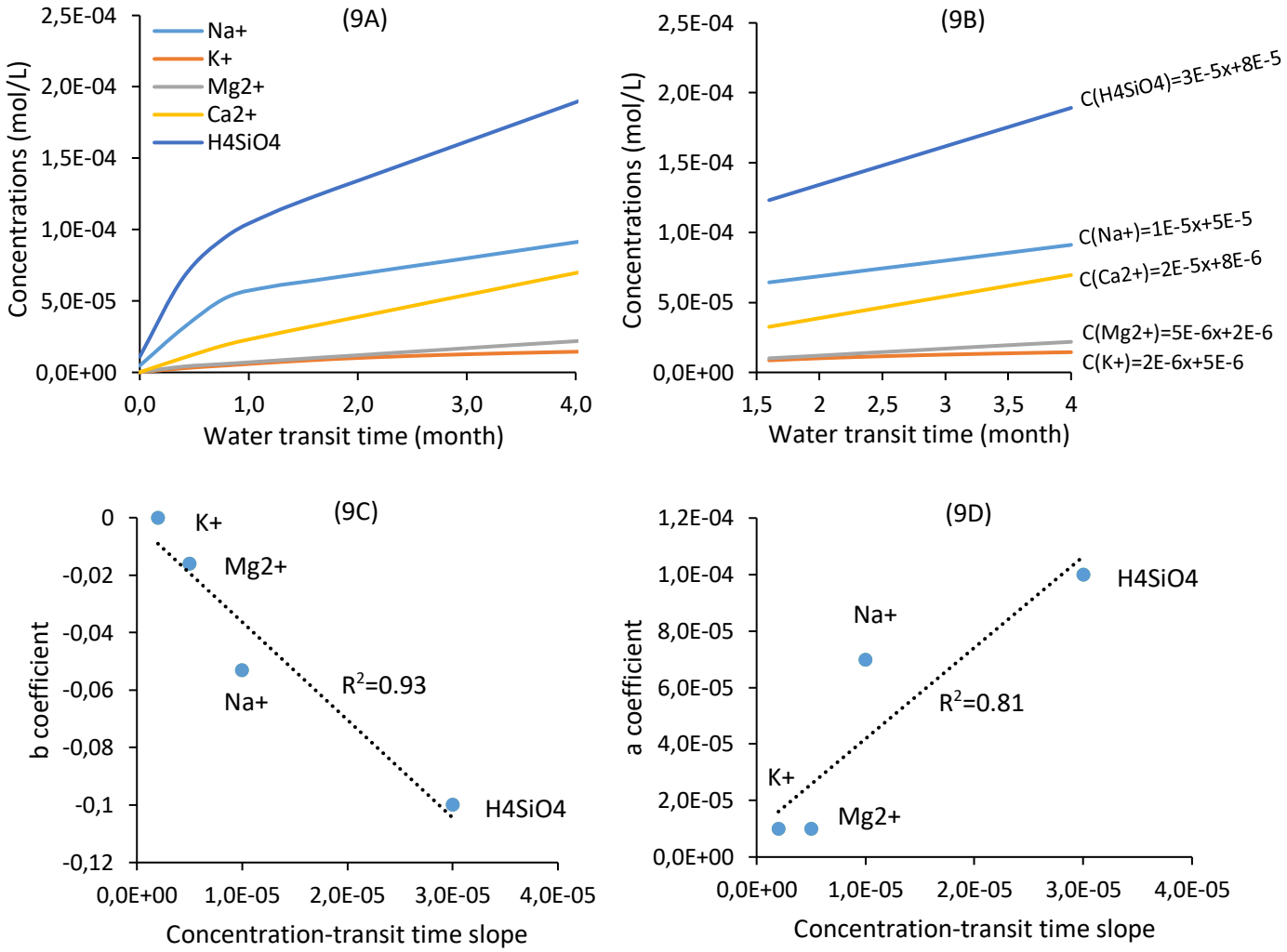
(9A)
Concentrations (mol/L)
Water transit time (month)
Na+
K+
Mg2+
Ca2+
H4SiO4
(9B)
C(H4SiO4)=3E-5x+8E-5
C(Na+)=1E-5x+5E-5
C(Ca2+)=2E-5x+8E-6
C(Mg2+)=5E-6x+2E-6
C(K+)=2E-6x+5E-6
(9C)
b coefficient
Concentration-transit time slope
R2=0.93
(9D)
a coefficient
R2=0.81

Figure 9

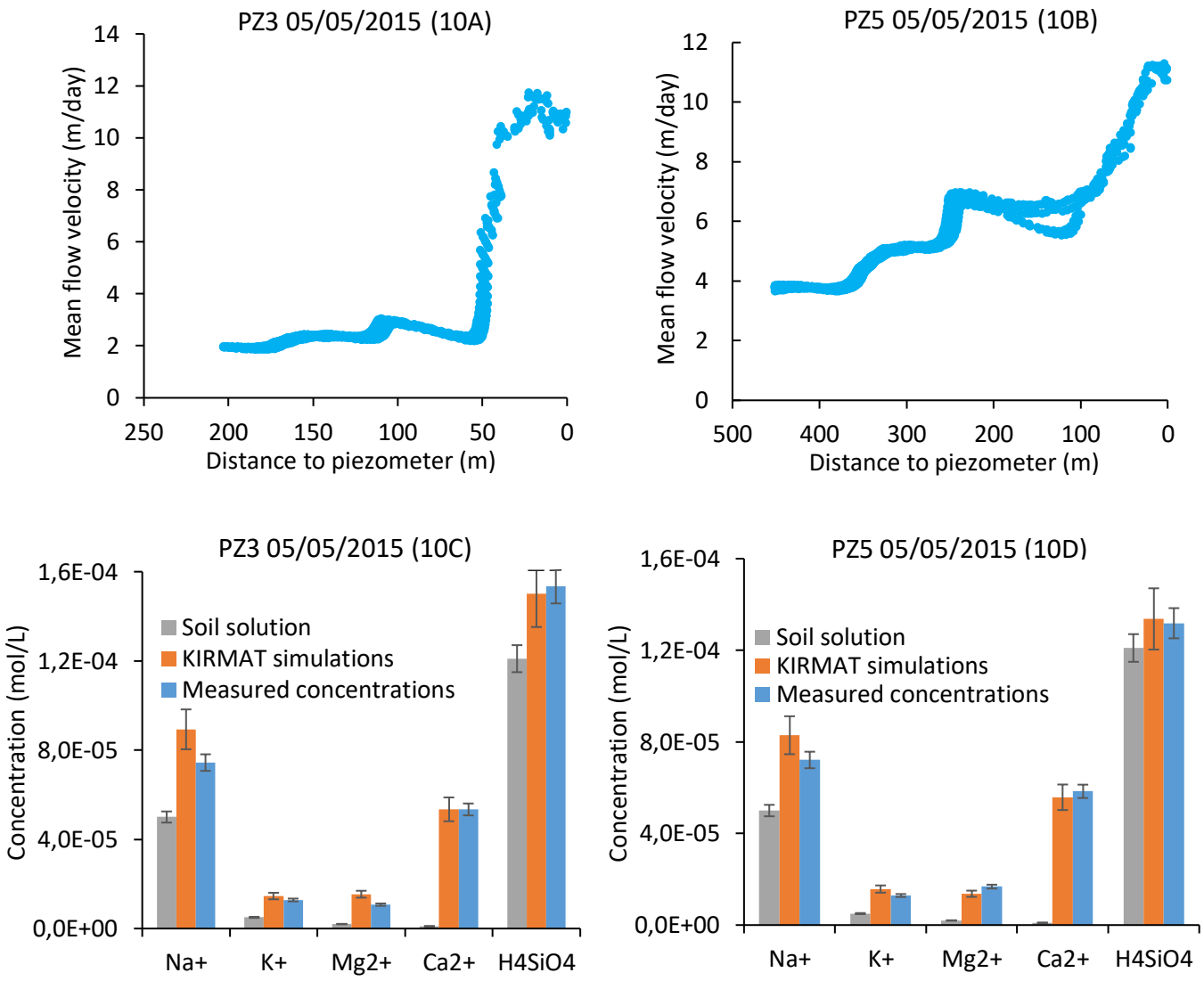
PZ3 05/05/2015 (10A)
Mean flow velocity (m/day)
Distance to piezometer (m)
PZ5 05/05/2015 (10B)
Mean flow velocity (m/day)
Distance to piezometer (m)
PZ3 05/05/2015 (10C)
Concentration (mol/L)
Soil solution
KIRMAT simulations
Measured concentrations
Na+
K+
Mg2+
Ca2+
H4SiO4
PZ5 05/05/2015 (10D)
Concentration (mol/L)
Soil solution
KIRMAT simulations
Measured concentrations
Na+
K+
Mg2+
Ca2+
H4SiO4

Figure 10

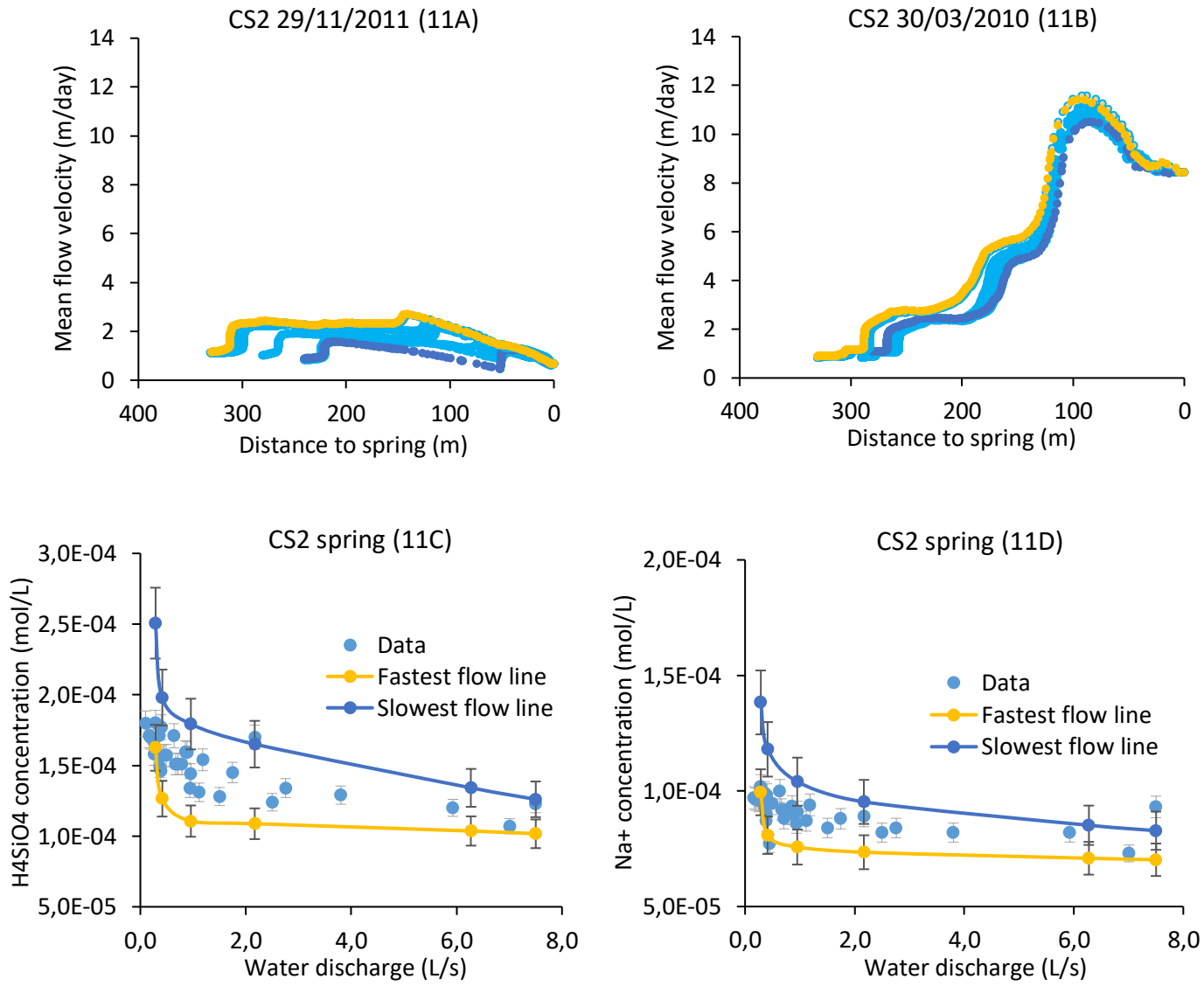
CS2 29/11/2011 (11A)
Mean flow velocity (m/day)
Distance to spring (m)
CS2 30/03/2010 (11B)
Mean flow velocity (m/day)
Distance to spring (m)
CS2 spring (11C)
H4SiO4 concentration (mol/L)
Water discharge (L/s)
Data
Fastest flow line
Slowest flow line
CS2 spring (11D)
Na+ concentration (mol/L)
Water discharge (L/s)
Data
Fastest flow line
Slowest flow line

Figure 11

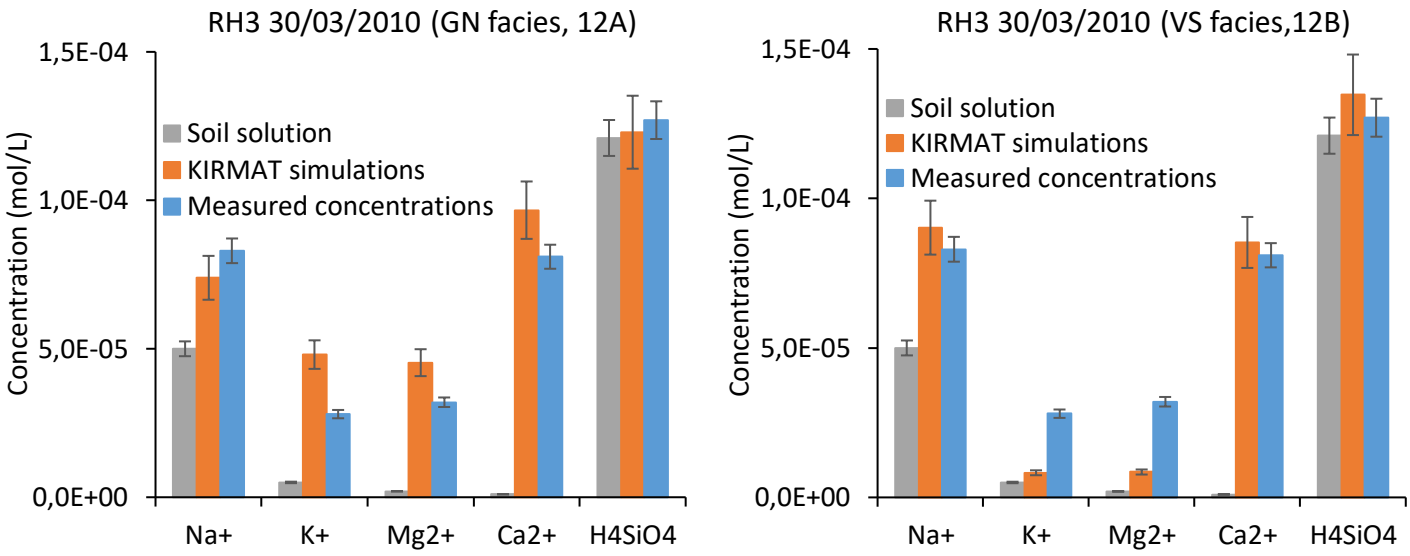
RH3 30/03/2010 (GN facies, 12A)
1,5E-04
1,0E-04
5,0E-05
0,0E+00
Concentration (mol/L)
Soil solution
KIRMAT simulations
Measured concentrations
Na+
K+
Mg2+
Ca2+
H4SiO4
RH3 30/03/2010 (VS facies,12B)
1,5E-04
1,0E-04
5,0E-05
0,0E+00
Concentration (mol/L)
Soil solution
KIRMAT simulations
Measured concentrations
Na+
K+
Mg2+
Ca2+
H4SiO4

Figure 12

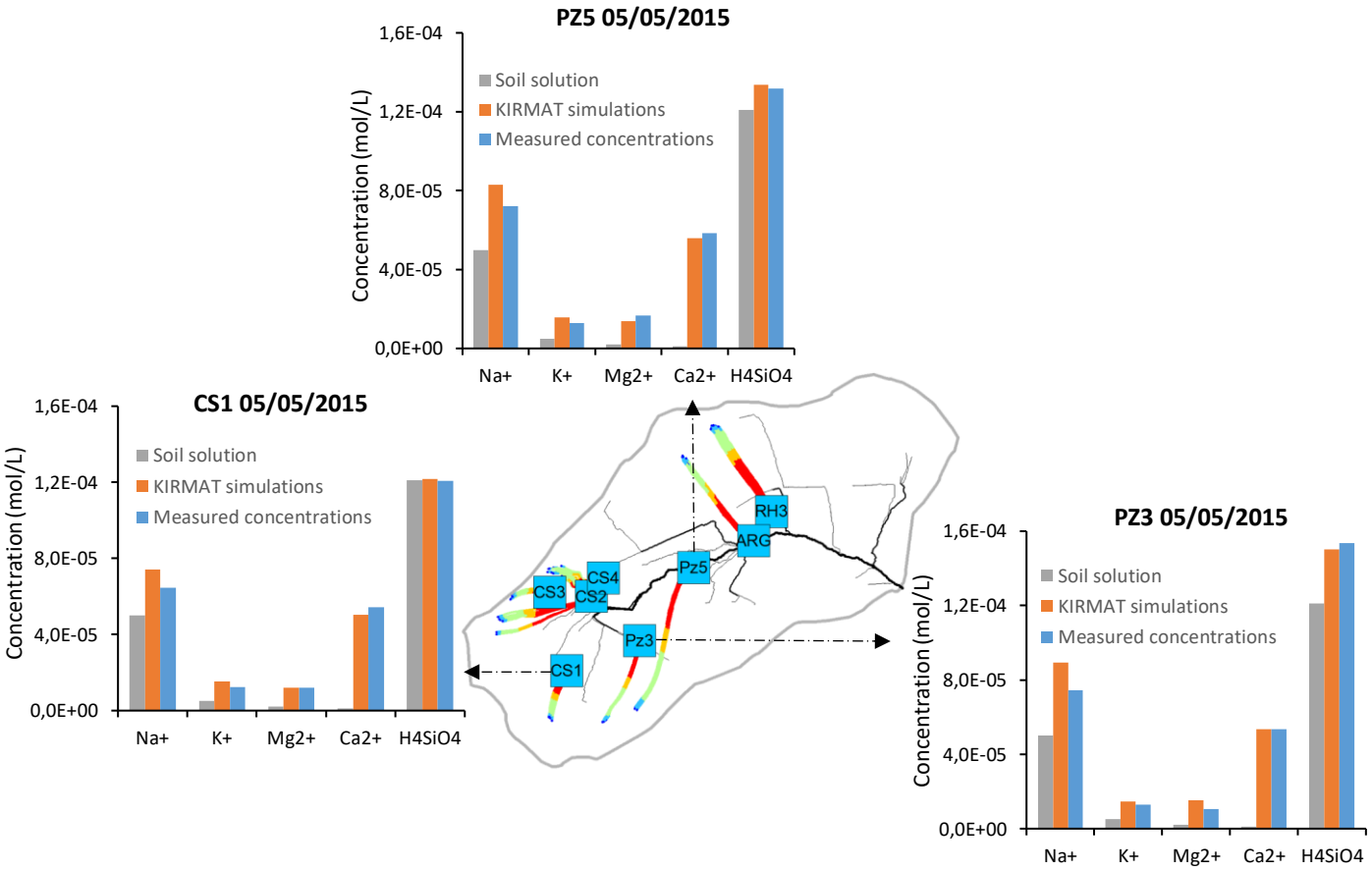
PZ5 05/05/2015
Concentration (mol/L)
1,6E-04
1,2E-04
8,0E-05
4,0E-05
0,0E+00
Soil solution
KIRMAT simulations
Measured concentrations
Na+
K+
Mg2+
Ca2+
H4SiO4
CS1 05/05/2015
PZ3 05/05/2015
RH3
ARG
Pz5
CS4
CS3
CS2
Pz3
CS1

Figure 13